Thermal Simulation Studies of a Cyclotron Liquid Target with Thick Niobium Window

Pedro Manuel Fernandes de Oliveira

Dissertation presented to the University of Coimbra in order to complete the necessary requirements to obtain the Master's degree in Engineering Physics.

FACULDADE DE CIÊNCIAS E TECNOLOGIA
UNIVERSIDADE D COIMBRA

Supervisor:

Prof. Dr. Francisco José Cerqueira Alves

Co-supervisor:

Prof. Dr. Sérgio José Coelho do Carmo

Julho de 2019

This project was developed in collaboration with:

ICNAS Produção Unipessoal Lda

Acknowledgements

Ao professor Francisco Alves, obrigado pela confiança e me ter dado a oportunidade de desenvolver um trabalho científico numa área que tanto me apaixona e pela orientação durante o desenvolvimento deste trabalho.

Ao Sérgio, obrigado pelo apoio e acompanhamento incansável. Obrigado por estares sempre disponível e me teres orientado e ajudado em tudo aquilo que precisei, esclarecendo toda e qualquer dúvida minha.

Aos professores do departamento de física da universidade de Coimbra, obrigado por me transmitirem a paixão pela física e todos os conhecimentos que adquiri nestes últimos anos.

Aos meus amigos e colegas de curso, que me acompanharam neste percurso. Obrigado por todos os momentos que passámos juntos, desde as sessões de estudo aos "cafés" noturnos. Um especial obrigado à minha família "FONITOS", obrigado pelos momentos mais divertidos que passei nestes últimos anos, levarei isso sempre comigo.

À Andreia, minha companheira em todos os momentos e principalmente em desafios como este. Obrigado pela tua paciência de anjo e pela tua ajuda em tudo aquilo que precisei. Foste a pessoa que me acompanhou do início ao fim nesta jornada, contigo tudo fica mais fácil e melhor. Obrigado pelo teu amor e dedicação, tentarei sempre retribuir cada gesto teu.

À minha família, pais e irmã, sem os quais nada disto tinha sido possível. Não há palavras que descrevam a minha gratidão, mas ainda assim deixo aqui uma tentativa de o fazer. Obrigado por todo o apoio e sacrifícios que fizeram para que eu pudesse ter o melhor percurso possível. Todos os meus feitos serão também sempre vossos.

Abstract

Liquid targets prove to be reliable and cost-effective on the radionuclide production. More recently, the interest on these targets increased due to its use for the radiometals production. The production yield of radioisotopes of cyclotron liquid targets is correlated and limited by the target thermal performance. High temperature increments of the target components during irradiation, resulting in their degradation, is one of the main observed problems. Helium and water are responsible for cooling the target, thus, improving its capacity to remove heat from the target system would lead to increase the proton current reaching the target and, consequently, improve the production yield. However, empirical data is almost non-existent due to the difficulty to measure the temperature of critical components of the target system, namely the target window and liquid target to be irradiated. Considering that few studies related with the thermal behaviour of liquid targets have been carried, there is a great need to study the liquid target system. This need becomes of greater importance due to the recent thick niobium windows implemented on radiometals production. To address this problem, thermal simulations combining fluid, nuclear and thermal physics were implemented to a better knowledge of the liquid target behaviour.

The aim of this work was to develop a Computation Fluid Dynamics (CFD) simulation model relying on Finite Element Methods (FEM), capable of simulating the thermal behaviour of a cyclotron liquid target. The heat deposition from a proton beam was calculated using the SRIM software. The software selected for the study of thermal physics was ANSYS-CFX.

In this work, a model that can simulate the thermodynamic behaviour of a liquid target was successfully conceived. The simulation model was used to study the main parameters that could influence the target thermal performance. The model was validated, comparing the obtained results with target cooling water temperatures measured experimentally. It was observed that the cooling water and helium mass flow rate strongly influence the temperatures of the window and liquid target. Thus, improving these parameters will lead to an improvement of the capacity to remove heat. On the other hand, inlet temperatures of the cooling water and helium proved to have a small effect on the temperature distributions.

***KEYWORDS*:** Liquid Target, Cyclotron, Niobium Window, Target Cooling, Thermodynamic Performance; CFD Simulation

Resumo

Os alvos líquidos permitem a produção de radionuclídeos, de forma eficaz e com baixo custo. Recentemente, a sua importância aumentou devido à sua utilização na produção de radiometais. O rendimento de produção de radionuclídeos em alvos líquidos de ciclotrão está diretamente relacionado e limitado pelo desempenho térmico do alvo. Um dos principais problemas associados com a irradiação de alvos líquidos são as altas temperaturas registadas nos diferentes componentes do alvo, o que pode levar à sua degradação. Hélio e água são os responsáveis pelo arrefecimento do alvo e melhorar a sua capacidade de remover calor, irá aumentar a corrente de protões que incide no alvo e, consequentemente, melhorar o rendimento de produção. No entanto, devido à dificuldade em medir as temperaturas dos componentes principais do alvo, nomeadamente na janela e no alvo líquido a ser irradiado, existem poucos dados experimentais disponíveis. Tendo em conta que existem poucos estudos sobre a desempenho térmico dos alvos líquidos, existe a necessidade de estudar os últimos. Esta necessidade ganha importância com a implementação de janelas "grossas" de nióbio na produção de radiometais. Com o intuito de resolver este problema e ganhar um conhecimento profundo do comportamento de alvos líquidos, foram desenvolvidas simulações que combinam a termodinâmica, mecânica de fluidos e física nuclear.

O objetivo deste trabalho foi desenvolver um modelo de simulação capaz de simular o comportamento termodinâmico do alvo líquido de ciclotrão, utilizando as ferramentas de Dinâmica de Fluidos Computacional (CFD) e o Método de Elementos Finitos (FEM). A deposição de calor proveniente do feixe de protões foi calculada utilizando o software SRIM. O software ANSYS-CFX foi o escolhido para a realização do estudo da termodinâmica.

O modelo desenvolvido permitiu de maneira eficaz simular o comportamento termodinâmico do alvo líquido. Este foi utilizado para estudar os parâmetros preponderantes capazes de influenciar o desempenho térmico do alvo. A validação do modelo foi realizada através da comparação dos resultados obtidos com medições experimentais da temperatura da água de arrefecimento. Foi observado que a temperatura da janela e do alvo líquido são influenciadas de forma significativa pelo caudal da água de arrefecimento e do hélio. Portanto,

a otimização destes parâmetros irá melhorar a capacidade de remover calor. No entanto, as temperaturas iniciais do hélio e da água de arrefecimento apresentam um efeito pequeno sobre as distribuições de temperaturas dos diferentes componentes do alvo.

PALAVRAS-CHAVE: Alvo Líquido, Ciclotrão, Janela de Nióbio, Arrefecimento do Alvo, Comportamento Termodinâmico, Simulação CFD

Contents

List of Figures

List of Tables

List of Abbreviations

^{18}F	Fluorine-18
^{18}O	Oxygen-18
^{66}G	Gallium-66
^{67}G	Gallium-67
^{68}G	Gallium-68
^{68}Zn	Zinc-68
BCA	Binary collision approximation
CFD	Computational Fluid Dynamics
FEM	Finite Element Method
Gr	Grashof number
ICNAS	Institute of Nuclear Sciences Applied to Health
MNCP	Monte Carlo N-Particle code
Nu	Nusselt number
PET	Positron Emission Tomography
PIG	Penning Ion Gauge
Pr	Prandtl number
Ra	Rayleigh number
RANS	Reynolds-averaged Navier-Stokes equations
RbCl	Rubidium-chloride
Re	Reynolds number
SST	Menter's Shear Stress Transport

TeO_2 Tellurium dioxide

$Zn(NO_3)_2$ Zinc nitrate

Chapter I. Introduction

One of the main methods to produce radionuclides rely on the proton beam irradiation of a cyclotron solid/liquid/gas target. For radiometals production, the solid targets usually enable the production of larger activities due to the improved cooling system and larger amount of enriched target material. However, the use of liquid target for radiometals production increased considering that it presents significant advantages, namely target material activation and a less complex pre- and post-irradiation manipulation (1). The liquid targets present a faster purification and labelling time and prove to be the cheapest option to produce radiometals like gallium-68 (^{68}Ga), due to the lower amount of enriched material required (2).

The production yield of radionuclides of cyclotron liquid targets is correlated and limited by the target thermal performance. The proton beam interaction with the target material could lead to its degradation due to heat generated, and consequent temperature increments. Most of the heat is generated at the target window and at the fluid to be irradiated (liquid target). Helium and water are the ones responsible for cooling the target. There is a concern to improve the capacity to remove heat that would reduce the temperature increments and allow to maximize the possible target current, while preventing the target damage. Therefore, there is an interest to better understand the thermal performance of the target, to avoid temperature-related incidents, in order to obtain the desired production yields. However, contrary to the solid target, few studies related with the thermal behaviour of liquid targets have been developed and, consequently, the empirical data is almost non-existent. This is a consequence of the difficult to measure the temperatures of the target window and the liquid target itself. To solve this problem, simulations combining fluid, nuclear and thermal physics could lead to a better knowledge of the liquid target behaviour.

For the particular case of ^{68}Ga, due to its chemical inertness, Niobium was chosen as the material of the window and the container enclosing the liquid target to be irradiated. The Niobium window has a large thickness that will lead to a significant heat generation due to the proton's energy deposition. Considering that the thermodynamic performance of this liquid target system is little explored, there is a great interest to study and to better understand its thermal behaviour. Therefore, this liquid target system will be the subject of present study.

This work focuses on the study of the thermal performance of the liquid target system. Computational Fluid Dynamic (CFD) and Finite Element methods (FEM) (3) are the most used methods (4) to study the thermodynamic behaviour and flow mechanics, and so, will be used to study and simulate the liquid target. In the following chapters, the theoretical knowledge regarding the nuclear and thermal physics involved with liquid targets system, as well as the software background, will be provided. At last, the description of the simulation model and the results discussion will be presented.

This thesis was developed at the Institute for Nuclear Sciences Applied to Health (ICNAS).

IBA Cyclone® 18/9 – Basic Principles

At the Institute of Nuclear Sciences Applied to Health (ICNAS, University of Coimbra), an IBA Cyclone® 18/9 (IBA, Louvain-la-Neuve, Belgium) (see Figure 3) is installed and used to mainly generate gallium-68 (^{68}Ga) and fluorine-18 (^{18}F) through the irradiation of liquid targets, along with other radionuclides in liquid and gas targets.

IBA Cyclone® 18/9 is a highly reliable cyclotron used to accelerate deuterons and protons, with fixed 9 MeV and 18 MeV, respectively. The cyclotron relies on electric and magnetic fields to induce an isochronous particles acceleration. At first, H^- ions are generated at the Penning Ion Gauge (PIG) source. The source consists of three electrodes, two cathodes at each end of a cylindrical anode (see Figure 1), with a magnetic field to ensure confinement of the electrons and promote the ionization of the hydrogen gas.

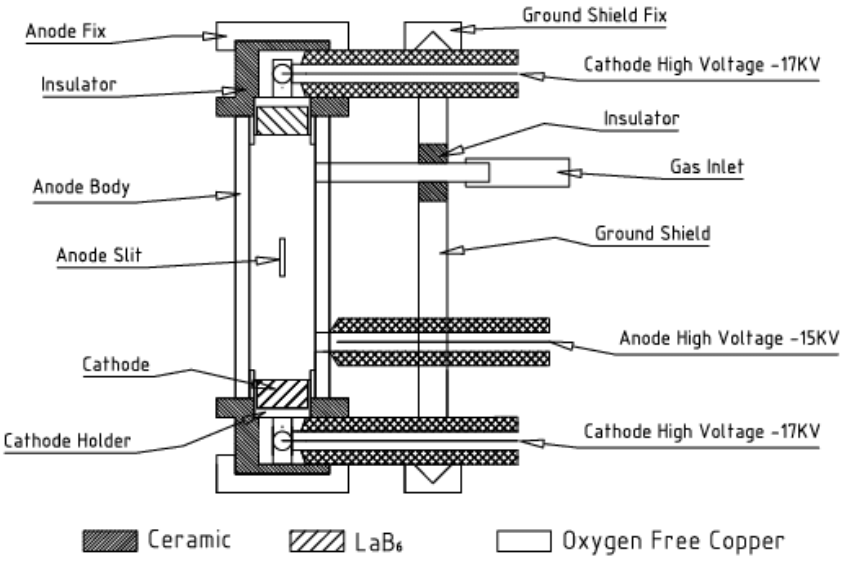

Figure 1 - Schematic representation of o PIG source. Adapted from (5).

Applying a high voltage at the electrodes results in the thermionic emission from the cathode which in turn, leads to the hydrogen gas ionization into H^- ions (plasma). H^- Ions are posteriorly accelerated by an electric field, $\vec{E}$, which is produced by the cyclotron radiofrequency system. A radiofrequency generator is responsible for creating an alternating voltage and changing the electrodes'(Ds) polarity, resulting in a proton energy gain through acceleration gaps between the Ds. Inside the latter the electric field does not have effect on the

ions. In the other hand, the magnetic field $\overrightarrow{B}$ guides the particles (see Figure 2), inducing a radial trajectory perpendicular to the magnetic field.

It is also necessary to ensure that the cyclotron operates under the resonance condition, which consists in guaranteeing that the frequency of the circular path revolution value is equal to the alternating electrical field frequency. Considering an ion with mass *m*, charge *q* and velocity *v*, moving on a plane perpendicular to the magnetic field, the magnetic field force is:

$$\left|\vec{F}\right| = \text{qvB} \qquad [1]$$

Considering that this force equals the centripetal force:

$$\frac{mv^2}{r} = \text{qvB} \leftrightarrow \frac{v}{r} = \frac{qB}{m} \qquad [2]$$

The frequency of the circular path revolution f_r is:

$$f_r = \frac{v}{2\pi r} = \frac{qB}{2\pi m} \qquad [3]$$

The alternating electrical field frequency must equal equation 3.

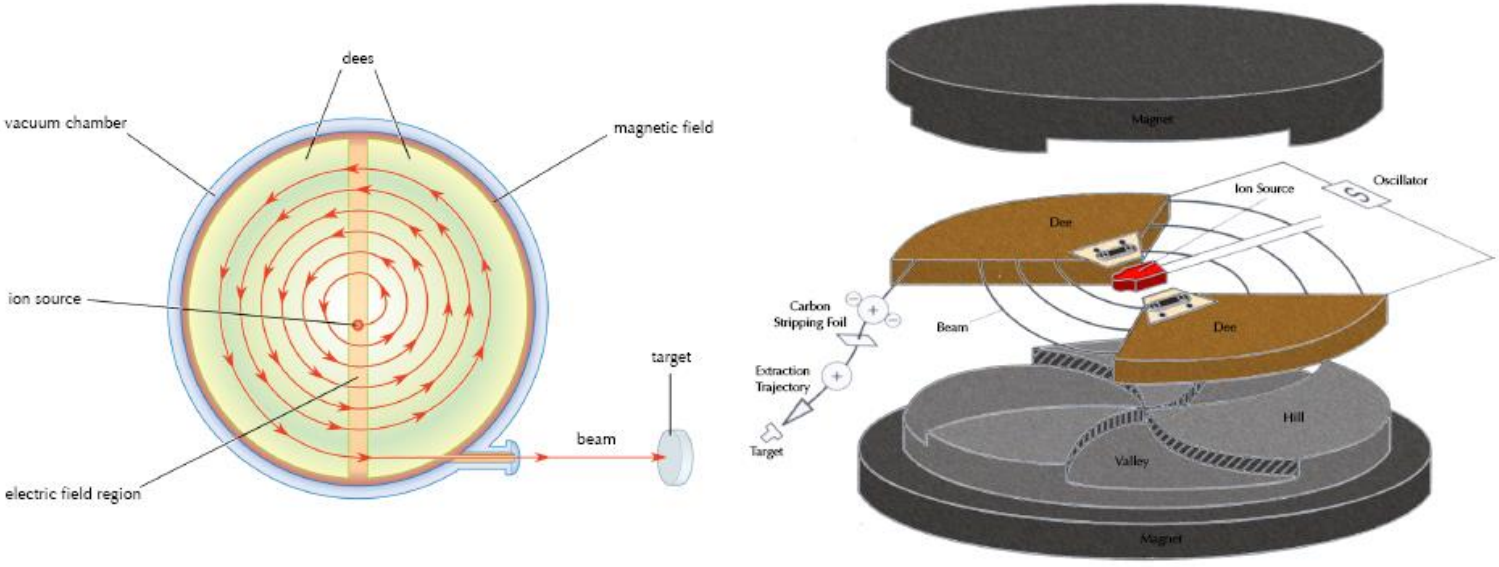

Figure 2 - Schematic diagram of a cyclotron depicting the position of the on source and magnets. A simplified view of the particle´s trajectory is also sketched. Adapted from (6).

The magnet presents a “deep valley” design, with four high magnet field areas called “hills” and four low magnetic field areas called “valleys”. This design is responsible for

the isochronous acceleration, where the magnetic field applied compensates the ions relativistic mass increase.

Finally, the H^- ions pass through a carbon foil with high collisional electron-detachment cross section for negative hydrogen ions, resulting in the electrons detachment from the H^- ions, converting the previously accelerated ions to protons (7). Considering that protons present opposite charge of the previously accelerated ions, an opposing Lorentz force is responsible for the extraction of the beam. Target-holders confine eight targets, that can be gaseous, liquid and solids.

Figure 3 - Picture of the IBA Cyclone® 18/9 from IBA Molecular installed at ICNAS.

Liquid Target System

Nowadays, the IBA F-18 Nirta® conical liquid target system (IBA, Louvain-La-Neuve, Belgium) (see Figure 4), presents a great yield for the production of the radioisotope ^{18}F, combined with an efficient thermal performance (8). It consists on a solid conical shaped niobium insert (see Figure 7), cooling water channels, the target windows, the helium cooling system, the aluminum diffuser and support (Figure 4).

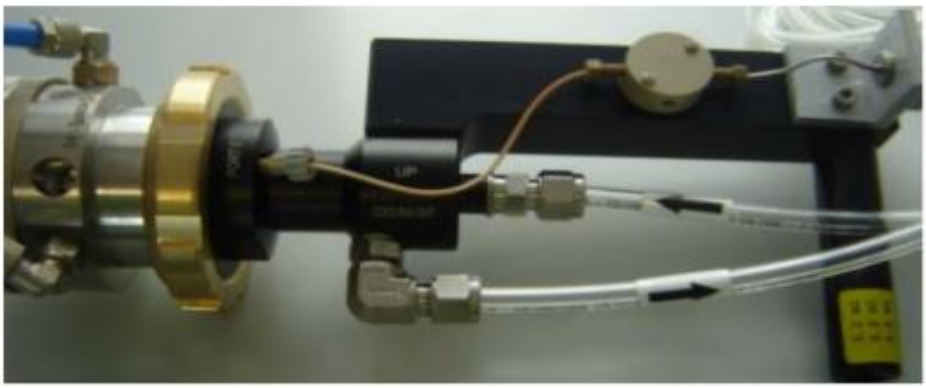

Figure 4 - Representative figure of the liquid target system. The arrows represent the water inlet and outlet. Adapted from (9).

The diffuser was designed in order to allow the cooling water to effectively flow near the conical insert and, posteriorly, exit the target system (Figure 5). In its turn the support takes the role to incorporate all the components while the conical insert enclosures the fluid to be irradiated. The first target window allows the confinement of the target system from the vacuum chamber inside the cyclotron while the second window allows enclosure of liquid target inside the conical shaped insert.

Figure 5 - Components of the niobium liquid target: a) conical target, b) target support and c) target diffusor. Adapted from (9).

The mechanisms responsible for removing the heat from the target system are the gaseous helium and cooling water. Helium flows between both windows, being capable of removing the heat generated. The choice of this gas is suitable for this process given its high thermal conductivity at 25ºC (0,142 W/m K) and low atomic weight (4,002692 u), to minimize energy lost before reaching the liquid target. An independent water-cooling circuit collects the heat from the target by convection heat transfer. Water with a mass flow rate of 3kg/min, enters

on the back of the target (Figure 6) and hits directly on the rear part of the conical insert, then flows between the niobium conical insert (Fig.5a) and the diffuser (Fig.5c), and following, between the diffuser and the support (Fig.5b) until it finally exits the liquid target system. The cooling water is continuously refrigerated by a water conditioner unit releasing the removed heat through a heat exchanger, controlled by a thermostatic three-way valve. Water impurities are removed trough reverse osmosis in order to maximize its purity and prevent electrical current flowing.

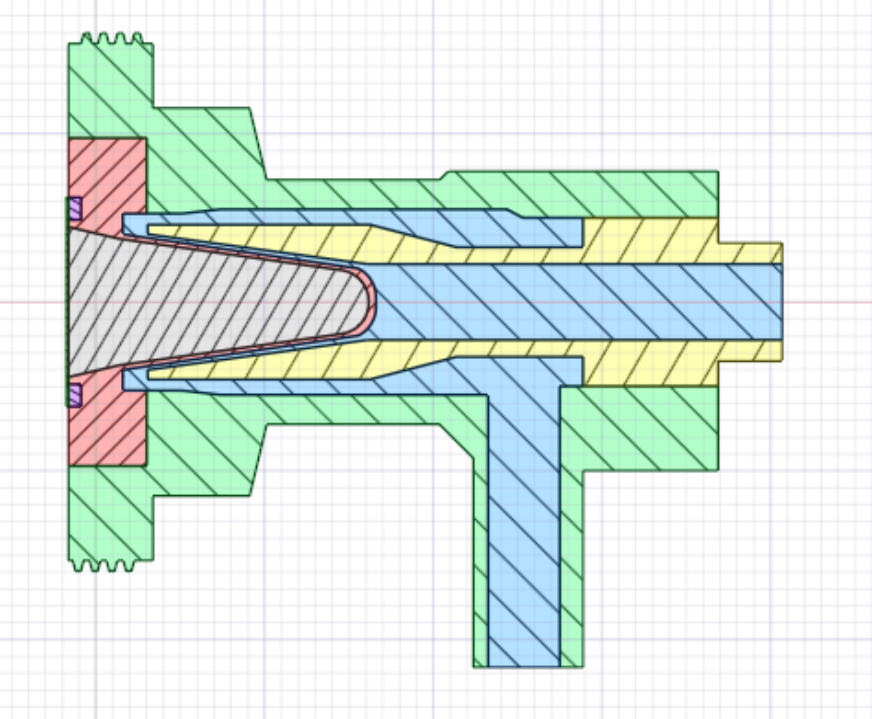

Figure 6 - Liquid target geometry domains designed in Inventor (Autodesk Inc., 2019): niobium conical target (red) and window (dark green), aluminium diffuser (yellow) and target support (light green), the nitrile O-Ring (purple), and also the fluid domains, water cooing channels (blue), and the liquid target domain (grey).

There are multiple designs and sizes available for the insert responsible for the liquid target enclosure (9). Both the volume of the target and the initially volume of liquid target are directly related to the pressure developed and with the activity output. These processes will be explained in the following chapters. The conical insert was designed to maximize the production yield and, consequently, use the minimum possible liquid solution while producing the maximum amount of radionuclides. It was also designed to present an effective cooling capacity and to reduce the amount of radionuclide impurities. The target material irradiation and consequent activation could originate undesired pollutants that could lead to contamination and affect the final yield. Since the irradiated fluid is located inside the conical insert, the latter

must present durability, resistant to high temperatures and high pressures, and an excellent thermal conductivity. These characteristics could lead to the increase the radionuclides production and to prevent the target material overheating and, consequently, its degradation and failure. Due to its chemical inertness for radionuclide production, suitable thermal properties (Table 1) and low thermal neutrons cross-section (10), the material of the IBA Nirta® target is pure niobium.

Table 1 - Niobium' properties at PTN. Retrieved from (http://periodictable.com/Elements/041/data.html).

Melting Point	2750,15 K
Specific Heat Capacity at Constant Pressure	265 J/kg K
Thermal Conductivity	54 W/m K
Density	8,57g/cm^3

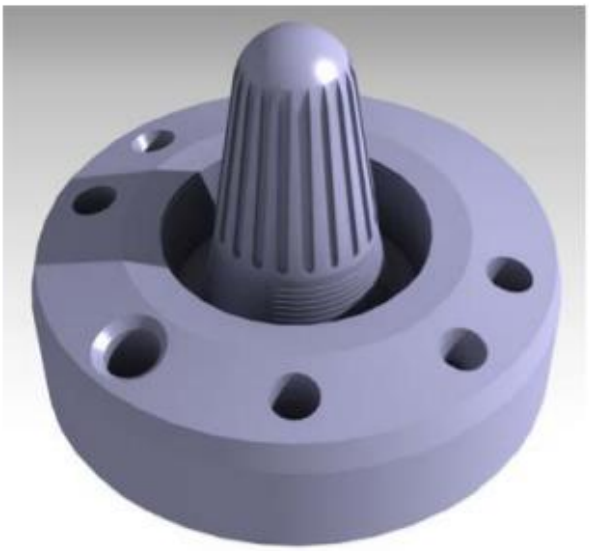

Figure 7 - Illustrative image of a Niobium conical insert. Adapted from (9).

Since the two main radioisotopes produced in liquid targets, at ICNAS, are ^{18}F and ^{68}Ga, both through the irradiation of the IBA F-18 Nirta® C8 (conical insert with a 36 mm cavity length and 3.7 ml volume), this design was selected for this study. The production of ^{18}F occurs via the ^{18}O(p,n)^{18}F nuclear reaction, in which the target is normally filled with Oxygen-18 (^{18}O) enriched water. For the production of ^{68}Ga, the target is filled with a zinc nitrate ($Zn(NO_3)_2$) based liquid solution, and the respective nuclear reaction is: ^{68}Zn(p,n)^{68}Ga.

The probability of a given nuclear reaction to occur is known as the cross section and it is dependent of the incident particle energy. This dependence is described by the nuclear reaction excitation function which in turn allows to visualize the protons energy range (optimum energy) corresponding to the maximum nuclear reaction cross section. Thus, it is desirable that the incident protons reach the liquid target with energies correspondent to the maximum cross section, in order to maximize the number of nuclear reactions of interest. However, it is also necessary to consider the excitation functions of undesirable nuclear reactions that could occur (impurities). In this case, it is important to make sure that the cross sections of these nuclear reactions are small for the energy of the protons reaching the liquid target. This way it is possible to minimize the presence of impurities on the output activity. Figures 8 and 9 show the excitation functions for the nuclear reactions: $^{18}O(p,n)^{18}F$ and $^{68}Zn(p,n)^{68}Ga$, respectively.

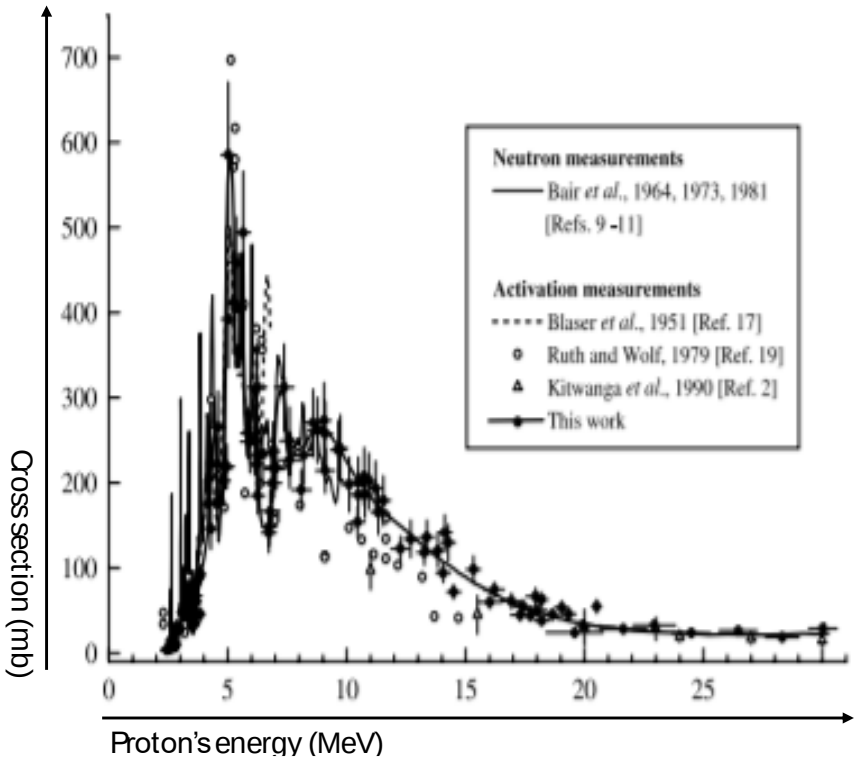

Figure 8 - $^{18}O(p,n)^{18}F$ excitation function. Neutron and activation measurements are shown Adapted from (11).

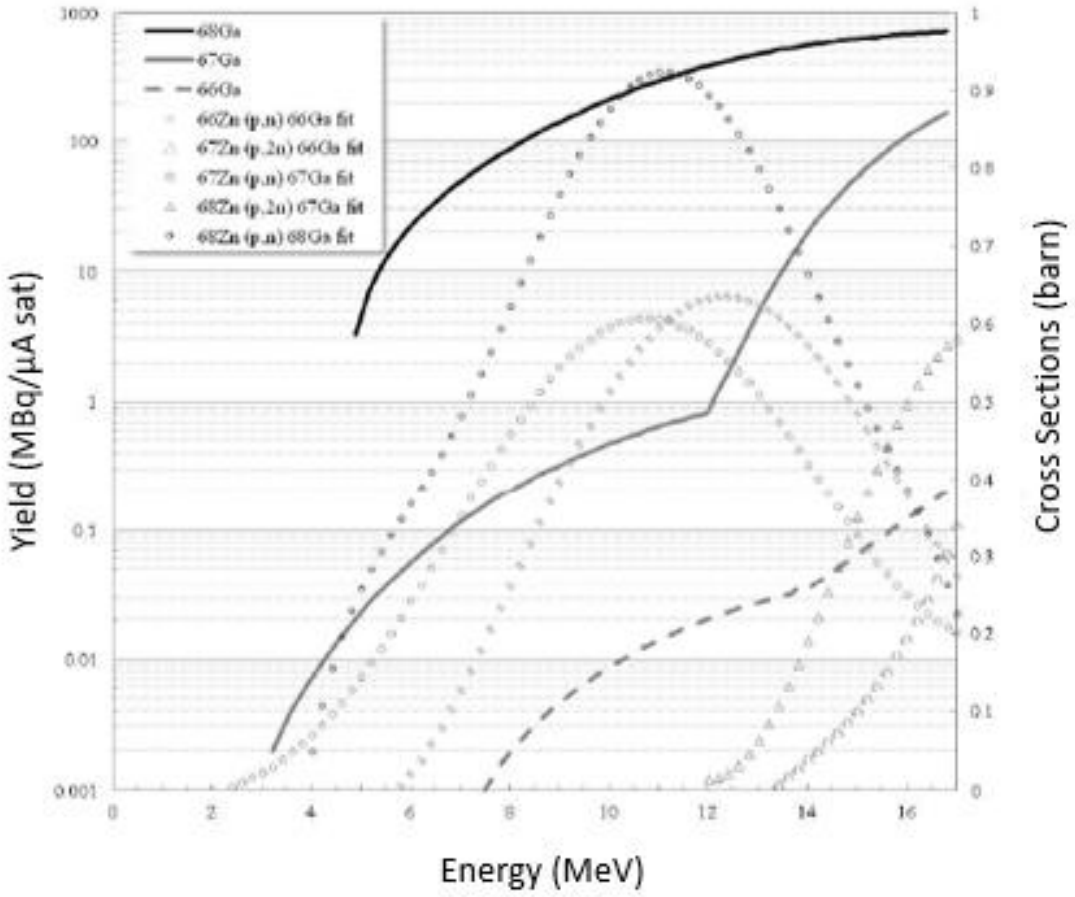

Figure 9 - Thick target yields at saturation (solid curves) for the production of gallium-66 (^{66}Ga), gallium-67 (^{67}Ga) and ^{68}Ga from a proton-irradiation of a liquid target with 200mg of zinc-68 (^{68}Zn) and excitation functions of the nuclear reactions of interest (open symbols). Adapted from (12).

Figures 8 and 9 show that larger cross sections are obtained in the 4-18 MeV energy range. Therefore, protons with energy below 4 MeV don´t contribute to the nuclear reactions of interest. It is then desirable that these proton´s deposit their energy on the rear (solid) part of the conical insert, i.e. generated heat in the niobium instead of the liquid target. This approach will not only reduce the heat generated in the liquid but also favor the heat removal by the cooling water hitting the back of the conical insert.

The incident proton beam of 18 MeV is progressively stopped within the liquid target due to its interaction with matter. After the beam is accelerated crosses a first conical collimator with a final diameter of 9.5 mm and crosses a second cylindrical collimator of 9.5 mm. Following, it passes through a Titanium window with a 12,5 μm length, whose purpose is to seal the liquid target system from the vacuum chamber. For the ^{18}F production, before reaching the liquid target protons go through a 35 μm thick Havar window (Figure 10) and for the ^{68}Ga

production the beam crosses a niobium window with thickness in the order of magnitude of hundreds of μm.

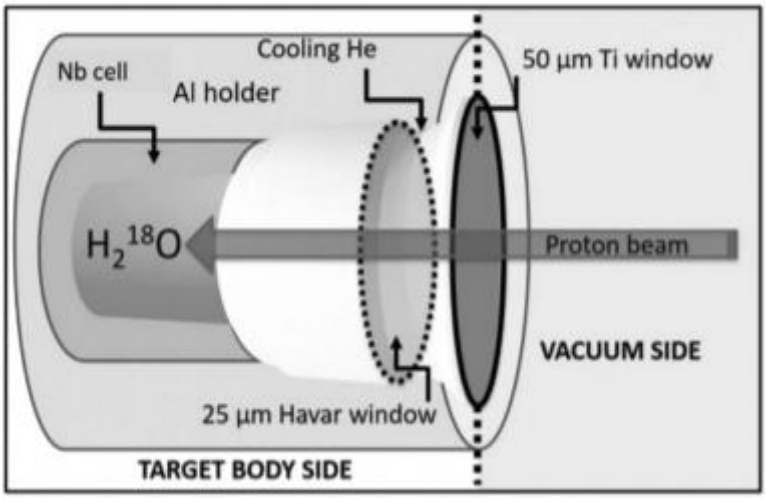

Figure 10 - Schematic representation of the target body and respective windows of a liquid target for ^{18}F production. Adapted from (13).

The beam interactions in the windows and the liquid target are responsible for the proton beam energy loss and consequently, the generation/production of heat. It is, therefore, important to understand how the protons interact with matter.

Energy Loss of Particles

Particles' energy loss is ruled by two main processes, inelastic collisions with atomic electrons and elastic scattering with the nucleus. In the former, the incident particles' energy is transferred to the atom, causing excitation or ionization, which are responsible for the major energy loss. The later process occurs less frequently resulting in a small energy transfer to the heavy nuclei.

When compared with electrons, protons are considerably heavier particles and therefore behave differently while passing through matter (14). Bearing in mind that inelastic collisions occur with a quantum mechanical probability, it is possible to describe the average energy loss per path' length unit, also known as stopping power. For heavy particles like protons, the stopping power is given by the Bethe-Bloch formula (14) (Equation 4):

$$-\frac{dE}{dx} = 2\pi N_a {r_e}^2 m_e c^2 \rho \frac{Z}{A} \frac{z^2}{\beta^2} \left[\ln\left(\frac{2 m_e \gamma^2 v^2 W_{max}}{I^2}\right) - 2\beta^2 - \delta - 2\frac{C}{Z}\right] \quad [4]$$

where N_a is the Avogadro's number, r_e the classic electron radius, m_e the electron mass, c the speed of light in vacuum, ρ the density of the absorbing material, Z the atomic number of the absorbing material, A the atomic weight of the absorbing material, z the charge of incident particle in units of e, β the v/c of the incident particle, v the particle's velocity, I the mean excitation potential , δ the density correction and W_{max} the maximum energy transfer in a single collision (Equation 5):

$$W_{max} = \frac{2 m_e c^2 \eta^2}{1 + 2s\sqrt{1 + \eta^2} + s^2} \quad [5],$$

$$s = \frac{m_e}{M} \quad [6],$$

$$\gamma = 1/\sqrt{1 - \beta^2} \quad [7],$$

$$\eta = \beta.\gamma \quad [8].$$

Furthermore, the proton beam can also be modelled as a 2D Gaussian function in order to allow a better approximation of the beam energy deployment:

$$f(x) = \frac{1}{2\pi\sigma_x\sigma_y} \times \exp\left(\frac{-(x - x_0)^2}{2\sigma_x^2}\right) \times \exp\left(\frac{-(y - y_0)^2}{2\sigma_y^2}\right) \quad [9],$$

where σ_x and σ_y are the standard deviations and x and y the spatial coordinates considering that the beam travels on the z direction.

Charged particle's energy loss during the passage through matter is strongly related to $\frac{1}{v^2}$, where v is the proton's velocity. As the heavy particle slows down in matter, the energy loss is also influenced. Consequently, the quantity of energy deposited per length' unit is greater at the end of the path, due to the fact that the particle energy is closer to the medium energy, making the interaction between them more likely. The stopping power of a heavy particle as a function of its position along the penetration depth is known as the Bragg curve (14) (Figure 11). The heat generated in the liquid target is ruled by this relationship between penetration depth and energy deposition. This point will be deeply explained in the following chapters.

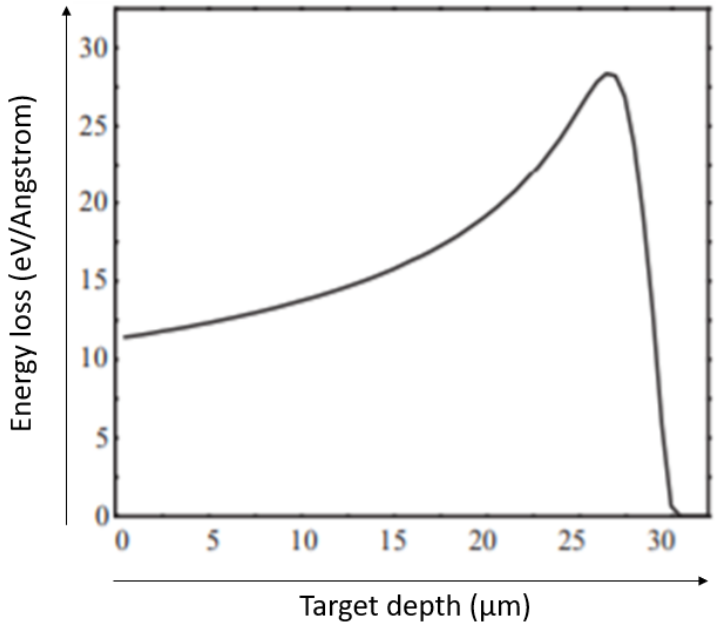

Figure 11 - Stopping power for 5 MeV alpha particles in a CR-39 Detector, calculate by SRIM software. Adapted from (15).

The Niobium conical-shaped target was designed so that the Bragg peak of the proton beam matches the very end of the target under typical irradiation conditions, ensuring that the beam deployed energy matches the excitation function region of interest. This is directly related with the liquid inside the target cavity since its density influences the beam energy loss through its path. This particularity will be explored in the following chapters.

Due to the complexity of Bethe-Bloch formula, it is helpful to use a software to calculate the proton beam energy density profile. Therefore, the energy deposition on the windows and liquid target is estimated using the Stopping and Range of Ions in Matter (SRIM) software (16). SRIM calculates the transport of ions in matter, using statistical algorithms and the Monte Carlo method of binary collision approximation (BCA). BCA (17) assumes that ions travel in a straight path, through a sequence of independent collisions , neglecting the energy loss for collisions with the nuclei. The software is based on the Bragg's rule and the Bethe-Bloch theory, presenting a reliable estimative of the stopping power of the particles tested. SRIM assumes that ions jump between calculated collisions, where the ion and the atom are governed by Coulomb collision, but also considers the interactions of the overlapping electron shells.

The most frequent applications of the software are the determination of the range of a beam of particles, its energy deposition over a material and sputtering (18). In 2013, a 3-D

graphic tool was introduced, making it possible to visualize the energy and position volumetric distribution of the particles. Its high precision and great variety of tools make SRIM suitable for the study of energy deposition of a proton beam on a cyclotron target application.

The Heat Transfer Problem

Fundamentals of Heat Transfer

Heat transfer is ruled by three mechanisms - conduction, convection and radiation. Conduction and convection need a medium to propagate and are proportional to the number of molecules. The molecules energy is related to its random translational, internal and vibrational motion. Higher the temperature, higher the molecules energy. Energy is transferred on molecules collisions, being transferred from molecules with higher molecular energy to the ones with less energy, resulting in a heat transfer in the direction of decreasing temperature. Regarding conduction, for gases and liquids, the energy transfer is enhanced by the collisions associated with the random molecular motion, and for solids, the lattice vibrational motion (phonons) is the main responsible for the heat transfer, where for good electrical conductors, it also occurs due to the translational motion of free electrons.

For conduction, the heat transfer rate is expressed by:

$$\frac{dQ_{cd}}{dt} = - k_t A \frac{\Delta T}{L} \quad [10],$$

where Q_{cd} is the conduction heat, k_t thermal conductivity, A the area, ΔT the temperature difference and L the length.

Heat transferred by convection is defined by the random molecular motion but also by the macroscopic motion of the fluid, where an aggregate of molecules transports the energy through its motion. Whenever a fluid is in contact with a surface with different temperature heat is transferred by convection. Convection can arise in two different situations *forced* convection is caused by external means, like compressed helium flowing past the target window, while *natural* convection occurs when temperature variations result in fluids' density differences,

inducing buoyancy forces. The rate equation for convection assumes the following form, known as Newton´s law of cooling (19).

$$\frac{dQ_{cv}}{dt} = h_c\, A\, (T_{surf} - T_w) \quad [11],$$

where Q_{cv} is the convective heat, h_c is the convective heat transfer coefficient, T_{surf} and T_w are the surface and fluid temperatures, respectively.

It is also important to consider the convection processes associated with the phase change, namely, boiling and condensation, where heat is transferred from or to the fluid without influencing the fluid temperature. This is known as latent heat. For boiling is characterized as the energy needed to overcome de attractive forces between molecules and for condensation represents the energy released in the change to a state with lower thermal energy(20). Also, the thermal conductivity of the liquid and respective gas is considerably different. Therefore, the phase change and consequently the presence of both phases will strongly influence the heat transfer inside the system.

Convection situations are defined by multiple fluid and flow properties, such as density, viscosity, specific heat and thermal conductivity. Prandtl (Pr) (Equation 12), Nusselt (Nu) (Equation 13), Reynolds (Re) (Equation 14), Grashof (Gr) (Equation 15) and Rayleigh (Ra) numbers present ratios between the main characteristics of fluids, serving as metricstoevaluate the fluid state.

Prandtl number defines the ration between the viscous and thermal diffusion rate:

$$Pr = \frac{c_p\, \mu}{k_t} \quad [12],$$

where k_t is the thermal conductivity, μ the dynamic viscosity and c_p the specific heat.

Nusselt number represents the ratio between convective and conductive heat transfer:

$$Nu = \frac{h_{cv}\, L_c}{k_t} \quad [13],$$

where h_{cv} is the convective heat transfer coefficient and L_c is the characteristic length.

Reynolds number represents the ratio between inertial and viscous forces:

$$Re = \frac{\mu L_c}{\lambda} \quad [14],$$

where μ is the dynamic viscosity and λ the kinematic viscosity.

The regime of the flow is determined by the Reynolds number, either being laminar, if Re<2300; transient, if 2300<Re<4000; or turbulent, if Re>4000.

Grashof number represents the ratio between buoyancy and viscous forces:

$$\mathrm{Gr} = \frac{D^3\ \rho^2\ g\ \Delta T\ \beta}{\mu^2} \quad [15],$$

where D is the diameter of an isothermal cylinder, ρ the density of the fluid, g the gravitational acceleration, ΔT the temperature difference between the fluid and the surface, β is the coefficient of volume expansion of the fluid and μ the dynamic viscosity.

All matter with non-zero temperature emits thermal radiation due to the continuous changing in electron configuration of atoms (21). In this case, the heat transfer occurs through electromagnetic waves transport and, therefore, does not need a medium to propagate. The black body states the reference for how efficient the emission of the body is, with values of emissivity in a range of 0≤ε≤1. According to the Stefan-Boltzmann law (Equation 16), the power emitted of a surface of a non-black body to its surroundings is:

$$E_r = \varepsilon\sigma(T_{surf}^4 - T_{surro}^4) \quad [16],$$

where ε is the emissivity, σ is the Stefan-Boltzmann constant, and T_{surf} and T_{surro} the surface and surroundings temperature, respectively.

The Stefan-Boltzmann law can also be translated in terms of the heat transfer from the surface:

$$\frac{dQ}{dt} = \varepsilon\sigma A(T_{surf}^4 - T_{surro}^4) \quad [17].$$

Target Thermal Performance

The heat transfer mechanisms mentioned on the previous section, dictate the heat and temperatures distribution on the solids and fluids of the liquid target system. The energy deposited by the beam generates a great amount of heat, on both the windows or the liquid

target. Since there are no studies about the heat effect on the niobium window used on the recent ^{68}Ga liquid target system, there is the need to study the heat dispersion on the Nb window. Also, the latter presents a larger thickness when compared with the Havar window used on ^{18}F irradiation, which consequently will increase the energy deposited by the beam. Thus, it is crucial to study the heat generated at the Nb window which will be the focus of the current work.

The heat generated in the target window is transferred to the cooling helium and to the liquid target, by convective heat transfer. Also, the heat generated in the liquid target is transferred by convection to the niobium conical insert and, consecutively, to the cooling water, especially on the rear part of the target where the temperature difference between the surface and the coolant is larger. This effect results from the large energy deposited per volume, on the location coincident with the Bragg peak. The generated heat at the window and liquid target is related to the initial energy of the beam, which is always 18MeV for this case, and to the proton current.

The heat generated by the beam energy deposition, increases the liquid target temperature, eventually resulting in its local evaporation. In its turn, the cooling water effect on the conical target wall will decrease the wall temperature leading to steam condensation. Hence, there will be the presence of steam in the beam path and liquid water on the surroundings of the conical insert. Since the conical insert is closed, its volume remains constant and the mass conservation of the liquid target is guaranteed. Therefore, the average density of the liquid target is constant. However, due to the presence of two distinct phases, steam and liquid water, the density will vary considerably along the liquid target domain. Since the phase change results from the generated heat, the density distribution of the liquid target will vary with the amount of local heat generated. On the other hand, as can be seen on Bethe-Bloch formula, the beam range and local deposited heat along its path is dependent on the density. The continuous variation and interdependence between density and beam deposition' energy profile will lead to a non-steady problem. Therefore, to accurately describe the energy deposition inside the target it is necessary to consider the variation with time of the density distribution and the energy deposition profile.

The IBA® niobium target can sustain a maximum pressure of about 40 bar, due to its mechanical strength. It is mandatory that the system presents a good capacity to effectively

remove the heat generated or else the pressure inside the target will exceed the limiting value, which will lead to the target window rupture and consequently, result in the target failure. The relationship between the proton current, I_p, and the target pressure is exponential. This relies on the fact that, beyond a certain I_p current threshold, the heat generated is superior to the system capacity of removing heat. Allied with the effect of the phase change occurring inside the target, where the evaporation rate increases with the generated heat. The larger number of gaseous molecules colliding with the wall container will also reflect in a pressure increase. It is also important to notice that the initial volume fraction of liquid water will present an effect on the pressure developed inside the target. If the volume occupied by the liquid increases, the gas molecules have less free remaining space to move, which will increase the molecules collisions with the container walls.

For a typical ^{18}F irradiation, the target with is filled with 3000 ml of ^{18}O enriched water. The corresponding pressure/current dependence is represented on Figure 12.

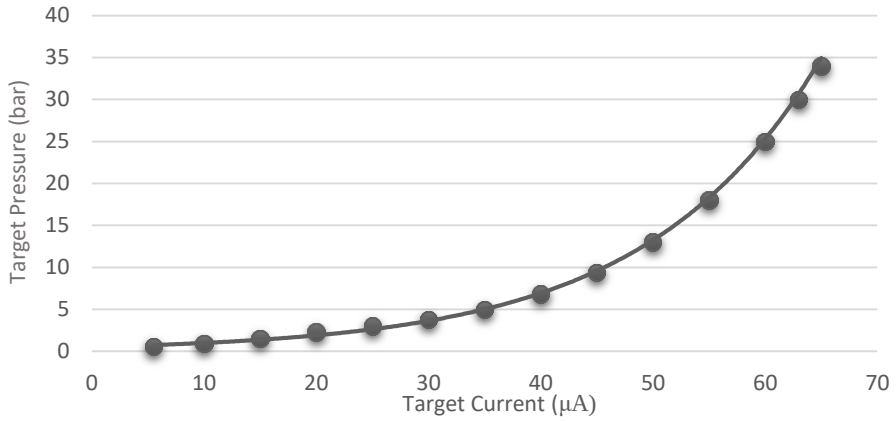

Figure 12 - IBA F-18 Nirta® - Target Pressure in function of the Target Current, for a ^{18}F irradiation with the target filled with 3 ml of ^{18}O enriched water.

With the target completely filled with 3,7 ml of enriched water, the maximum safety pressure is reached for a much smaller proton current, as can be seen on Figure 13.

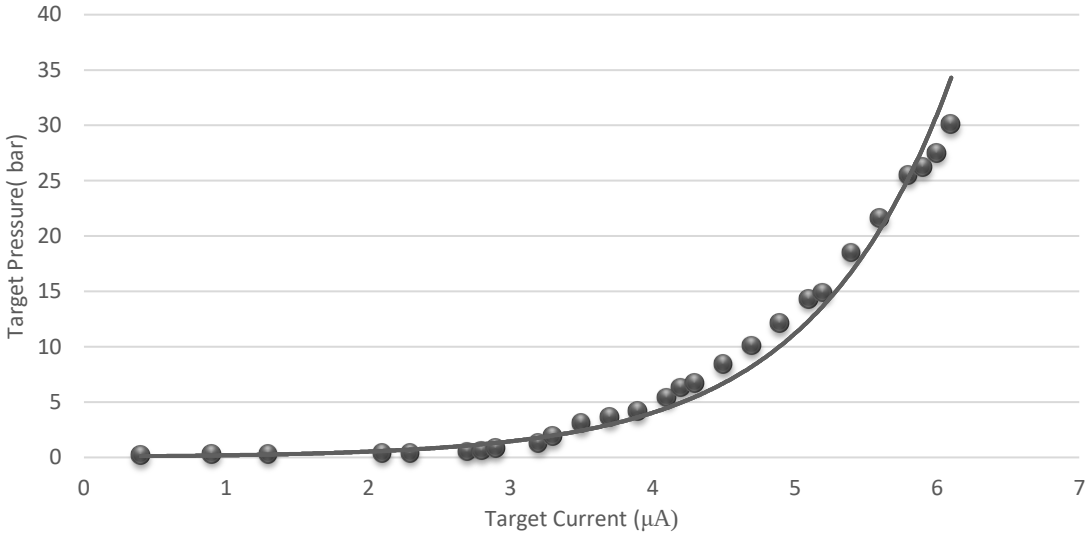

Figure 13 - IBA F-18 Nirta® Target Pressure in function of the Target Current for a ^{18}F irradiation with the target filled with 3,7 ml of ^{18}O enriched water.

The power deposited by the proton current, I_p, considering the beam energy, E_p, can be approximately calculated by:

$$\frac{dE}{dt} = I_p \times E_p \quad [18].$$

Equation 18 is not the most accurate approach to calculate the power of the beam, yet it is sufficiently close to the real value. As an example, for a typical Cyclone18/9 irradiation with a proton current of about 60 μA and the proton beam energy of 18 MeV, relying on equation 18, the deposited power is 1080 W. This corresponds to the power deployed in the target system, thus, it is crucial to effectively remove the heat generated by the proton current in order to prevent the target system failure. Helium flowing next to the window and the cooling water flowing on the surface of the conical insert are responsible for removing heat from the system.

The quantity of produced radionuclides is proportional to the number of nuclear reactions, which in turn is proportional to the proton current reaching the target. Also, the pressure deployed in the target increases with the target current. Thus, there is the balance between maximizing the proton current reaching the liquid target and keeping the target pressure below the safety value. Increasing the capacity of the system to remove heat, will reduce the pressure, allowing to increase the target current and consequently, produce more radionuclides. It is then clear that the radionuclide production limiting factor relies on the

thermal performance of the liquid target system, thus, it is mandatory to find mechanisms which allow to improve the helium and cooling water effect on the system.

The capacity to remove heat is influenced by multiple parameters of the target system. The convective heat transfer is proportional to the temperature difference between the surface and fluid and to the heat transfer coefficient, which in turn is proportional to coolant mass flow rate (22). Also, the heat transfer is correlated with the thermal conductivity of the target materials and their design (9). Therefore, the latter and the cooling water and helium parameters could possibly influence the capacity to remove heat. Hence, a CFD (Computational Fluid Dynamics) simulation of the thermal performance of the target implementing all these features will make possible to study the capacity to remove heat and also its possible improvement.

Computational Implementation of the Liquid Target

Computational Fluid Dynamics (CFD)

In the 1960s, due to the emerging of computer technology combined with the growing necessity of a depth knowledge of fluid dynamics and heat transfer, CFD arose. With the increase of the computational power, this technique spanned over a wide number of industrial applications (23), (24), (25). Through the application of governing and discretization methods, this tool allows to achieve very accurate solutions resulting in both shorter simulation time and smaller costs (26).

Nowadays, with the development of algorithms and physic models, CFD is a standard method in several industrial applications as well as in countless processes of the engineering world. The wide range of fields cover building services, electronics, medical and safety applications, among others. Specifically, in nuclear engineering and design, CFD proves to be an accurate tool in the matter of safety, verification and validation techniques (27).

CFD describes momentum, heat and mass transfer making use of the Navier-Stokes differential equations (Equations 19, 20 and 22), combined with Finite Element Method (FEM), which will be further explained.

The Finite Element Method (FEM)

With the purpose of solving complex problems, the FEM method subdivides the global domain in individual elements, in a process called discretization (28). Elements can assume any geometric shape and the number of elements is proportional to the solution accuracy. For each element, a specific function is assigned. The degree of the function is proportional to the accuracy of the approximation to the exact solution (Figure 14). This function is traduced into equations and posteriorly, all element's solutions are assembled resulting in a global stiffness matrix. Lastly, boundary and initial conditions are imposed. The node values are determined once the algebraic equations are solved, and it is possible to obtain temperature, velocity and other variables of interest characterizing the system.

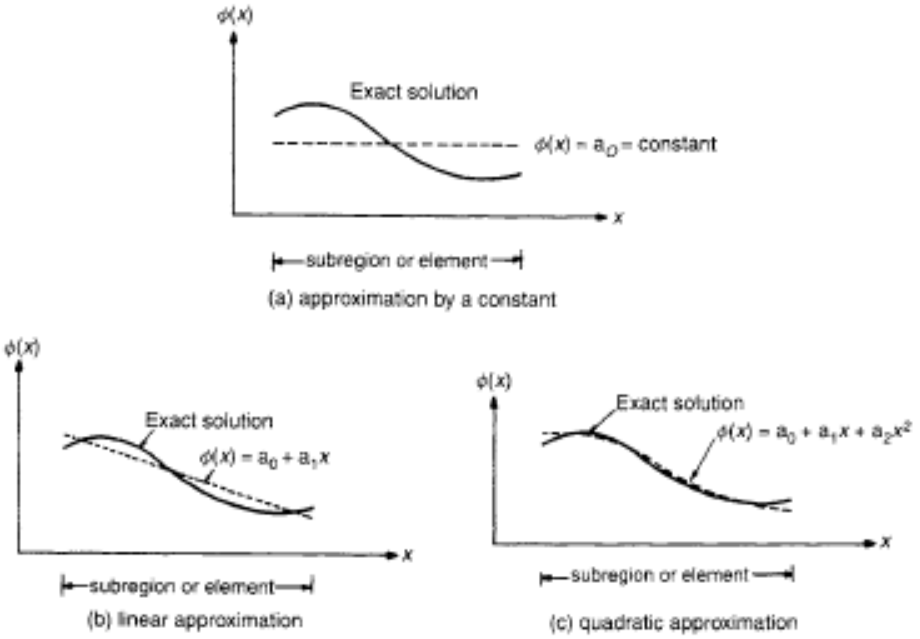

Figure 14 - Example of a FEM approach to several degrees' functions representing the behaviour of an element. Adapted from (27).

Nowadays computers allow to apply mathematical models to each element and their posterior assembling allows to obtain an approximated solution of a very complex problem. Many CFD software's, like ANSYS CFX (version 19.2; ANSYS, Inc., 2013), are based on FEM, which is an effective tool to simulate real physic phenomena, involving heat transfer, fluid flow, phase change and electromagnetic processes.

ANSYS CFX (v. 19.2, ANSYS, Inc.)

In the recent years, one of the most used CFD software in nuclear physics and industrial applications is ANSYS (ANSYS, Inc., 2013) (29), (30). Based on governing equations and FEM, the software allows accurate simulations of real-world problems. The software is composed of several tools, among which the ANSYS CFX. This latter is composed by four main models: CFX-Pre, CFX-Solver, CFX-Solver Manager and CFD-Post, which allow a sequential modulation of the CFD problem (Figure 15). ANSYS CFX is a robust tool, able to model steady and transient states involving structural, thermal and flow physics - such as laminar or turbulent flows, subsonic or supersonic flows, buoyancy, multiphase, chemical reactions and particle tracking.

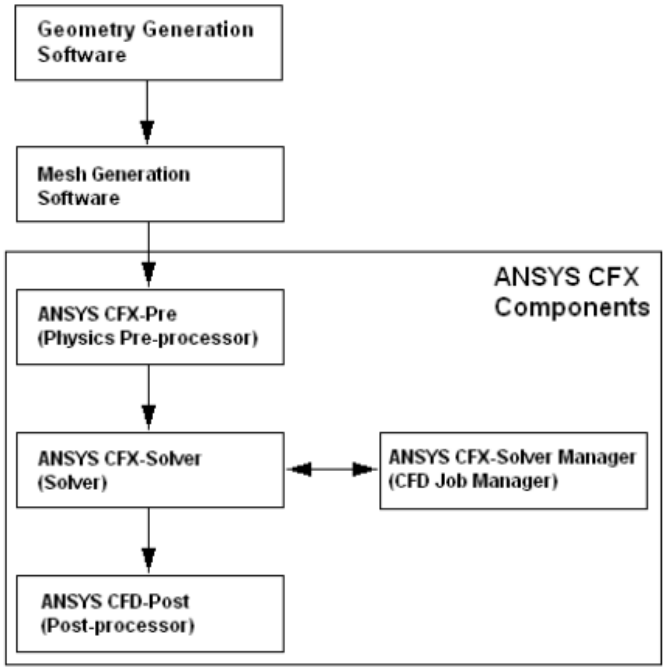

Figure 15 - Sequential steps in an analysis of a CFD problem, using ANSYS CFX. Adapted from (31).

The software is also composed by the SpaceClaim application which allows the design of the physical structure, where all the solids and fluid domains are defined, followed by the mesh generation (using the Mesh generation software tool), where the geometry domains are discretized in elements. These two tools are the first approach to the problem. It is, afterwards, in the Pre-processor that all the models, including turbulence, forces acting on the fluid, heat models, boundary and initial conditions, like temperature and velocity, are defined. After all the simulation parameters are established, the solution is calculated in an iteration step method, until convergence is reached. The exact solution is achieved when the residuals, which

measure the overall conservation of the system properties, achieve a pre-established value. It should be noted that in complex problems, oscillating residuals will appear in critical parts and it is not always possible to obtain such small residuals values. It is in this step that the differential equations resulting from the governing equations are solved. ANSYS allows the connection with an external solver to reduce the solution calculation time. Lastly, the Post-processor provides a complete interface to observe all the system variables. ANSYS CFX also presents compatibility with other software, namely software's implementing Monte Carlo methods to simulate nuclear processes, as an example, MCNPX (32) and DYN3D (33). Making it a perfect tool to combine a descriptive flow study with nuclear physics.

The solutions calculated by the software rely on the governing equations, which describe the variables spatial distribution and its evolution in time. Mass, momentum and energy conservation are guaranteed in three main equations. These represent the conservation laws of physics, establishing that mass is always conserved (equation 19), the rate of change of momentum equals the sum of all forces on a fluid (equation 20) and that the rate of change of energy equals the sum of the rate of the work done on the fluid particle and the heat addition (equation 22):

Continuity equation:

$$\frac{\partial \rho}{\partial t} + \nabla \cdot (\rho \, \boldsymbol{u}) = 0 \qquad [19],$$

where ρ is the density and $\boldsymbol{u}$ the velocity.

Momentum equation:

$$\frac{\partial (\rho \boldsymbol{u})}{\partial t} + \nabla \cdot (\rho \, \boldsymbol{u} \otimes \boldsymbol{u}) = -\nabla p + \nabla \cdot \tau + \boldsymbol{S_M} \qquad [20],$$

where $\boldsymbol{S_M}$ is the momentum source and τ is the stress tensor given by:

$$\tau = \mu(\nabla \boldsymbol{u} \; + (\nabla \boldsymbol{u})^{\boldsymbol{T}} - \frac{2}{3}\delta \nabla \cdot \boldsymbol{u}) \qquad [21],$$

where μ is the dynamic viscosity, $\boldsymbol{T}$ transpose matrix and δ the strain rate.

Energy equation:

$$\frac{\partial\,(\rho\, h_{tot}\,)}{\partial t} - \frac{\partial \rho}{\partial t} + \nabla \cdot (\rho\, \boldsymbol{u}\, h_{\boldsymbol{tot}}) = \nabla \cdot (\lambda\, \nabla \mathrm{T}) + \nabla \cdot (\boldsymbol{u} \cdot \tau) + \boldsymbol{u} \cdot S_M + S_E \quad [22],$$

where S_E is the energy source h_{tot} is the total enthalpy and is given by:

$$h_{tot} = h + \frac{1}{2}\boldsymbol{u}^2 \quad [23]$$

where h is the static enthalpy.

These equations are also known as the Navier-Stokes equations, in their conservation form. The variables present in these equations can be decomposed into an average value and its fluctuation. The decomposition introduces new unknowns that are associated to turbulence terms.

Turbulence

Most physic phenomenon's involving fluids present a turbulent behaviour, where inertia forces are significantly larger when compared to viscous forces, inducing strong fluctuations all over the fluid properties. Usually, Reynolds number (Equation 14) is applied to determine if the regime of the flow is laminar, smooth with adjacent layers, or turbulent, where flow properties are random and chaotic.

Eddying motions induce complex interaction between multiple coexistent fluids, involving heat, mass, and momentum properties (34). The random nature of this regime makes its simulation difficult and sometimes inaccurate, although indispensable to correctly describe the reality.

Turbulence Models

Several numerical methods and different models are available to predict turbulence effects (35). The numerical methods that comprise turbulence effects can be subdivided in three main groups, according to whether the time scale is in the order of magnitude of turbulent fluctuations or not:

Large eddy Simulation: Navier-Stokes equations are filtered leading to the rejection of small eddies, resulting in a focus on the larger ones. Small eddies are posteriorly solved on a sub-grid scale model. Due to the separated treatment of smaller or bigger scales, comparing

with the mesh, and to the unsteady nature of the flow equations, a great computation effort is needed.

Direct numerical Simulation: Mean flow and turbulence fluctuations are solved by the Navier-Stokes equations in spatial grids. These grids are sufficiently small to resolve the small turbulence fluctuations scale, however, the computational time and the memory requirement for this method is considerably large.

Reynolds-averaged Navier-Stokes equations (RANS): It uses time-averaged Navier-Stokes equations to resolve the effects of turbulence on mean flow properties, where small fluctuations exhibit average characteristics. On the other hand, the extra terms are treated on the time averaged (Reynolds-averaged) flow equations. The fact that these models work with time-averaged properties allows to present an accurate description for a wide number of turbulence cases, with more modest computational effort, makes them a universal choice for most flow simulations and the turbulence model chosen for the present work. RANS models can be classified according to the extra number of transportation equations that need to be solved, usually the number of extra terms used is two. ANSYS CFX allows the implementation of the two-equation turbulence models used to solve the extra terms:

***k*-ε model:** This model uses separated transport equations to solve turbulent kinetic energy, *k*, and turbulent eddy dissipation, ε (36). The model provides a good combination between accurate results and memory use. Therefore, and considering its strong robustness, it is considered the standard model for most industrial applications. The greatest disadvantages come for adverse pressure gradients, where the model predicts excess turbulent shear stress, and in modelling the turbulence near the boundary for no-slip walls.

***k*-ω model:** an alternative to the previous model, where ε is replaced by the rate of dissipation of kinetic energy, ω (37). In the presence of strong pressure gradients, most turbulence models fail to predict the flow separation from a smooth surface. When compared with k-ε model, this latter presents a more accurate modelling of the near wall interactions. The limitations of the k-ω model relies on the fact that it i sensitive to initial conditions allied to a difficulty to reach convergence.

Menter's Shear Stress Transport (SST) model: as k-ε and k-ω models are effective on turbulence modelling of free stream and near walls, respectively; SST provides a combination that removes the weaknesses of both models (38). This way it is capable of model adverse pressure gradients in boundary layers and pressure induced separation.

Hence, the turbulence modelling near the wall depends on the used model. Therefore, the heat transfer between the surface and the fluid, relies on the flow behaviour near the boundary, i.e., on the chosen turbulence model. As an example, the heat transfer from the conical insert to the cooling water is better modelled by the k-ω or SST turbulence models, due to the fact that both these models are suitable for modelling turbulence in the boundary layers.

Literature Review

CFD software, namely ANSYS-CFX, has been used in several works with the purpose to develop thermal analysis studies, namely simulations regarding nuclear targets.

Since it is impractical to measure the temperatures of the target window and conical insert, Trevor V.Dury (39) simulated the temperatures of the target window relying on a CFD simulation. CFX software was used to test the influence of the coolant mass flow rate on the window temperature, for a constant heat flux of $10^5 W/m^2$. Also, several simulation runs were made for diverse turbulence models and meshes with different number of elements. The simulation was validated comparing with experimental results and predicted an accuracy of $\pm$5%. This work allowed to conclude that increasing the bypass mass flow rate from 2,5 to 3kg/s, lowered the peak window temperature by 22ºC.

The thermal behaviour of a tellurium dioxide (TeO_2) target was modelled relying on the governing equations and the Finite Volume method (40). The heat flux and flow description were studied in order to verify if the geometry of the target satisfied the design criteria. SRIM software was used to study the protons stopping power, which allowed to determine the external heat source. The proton beam path was divided in 5 layers and the average deposited energy in each layer was multiplied by the proton current to obtain the deposited heat. Helium and water are responsible for cooling the solid target and were also

implemented. Considering all this, the temperature distribution was calculated. The results showed that the maximum temperature coincided with the Bragg peak.

A similar study for the thermal analysis of a Thallium (Tl) solid target was performed by N. Jung *et al.* (41). SRIM was used to calculate the energy loss of the proton beam in the target. Once again, the Tl layer was divided in 5 regions resulting in 5 heat sources correspondent to the average deposited energy. The simulations sensitivity for the major operational parameters was tested, such as the coolant temperature and mass flow rate and the proton incident angle. Although, both the coolant properties presented a small influence on the maximum target temperature, the incident angle proved to have a great effect. Finally, it was verified that the maximum target current increased linearly with the beam current.

To test the design of a power extraction reactor, a team of researchers carried out a thermal analysis of the target windows (42). FLUENT CFD software was used to calculate the maximum temperatures reached at the target windows as a function of the cooling inlet velocity and beam current. It was verified that the windows maximum temperature increased almost linearly with the beam current and that increasing the coolant inlet velocity from 1,1 to 2m/s resulted in a decrease of the maximum temperature of 469ºC. This way, it is clear that the coolant mass flow rate presents a strong influence on the window maximum temperature.

As previously mentioned, in order to correctly model the thermal empiric behaviour of the liquid target system, it is important to implement the coupling between the liquid target density variation and the beam deposition energy distribution. Several authors implemented a multi-physics coupling, using a Monte Carlo code to calculate the beam energy deposition energy profile and a CFD software to calculate the thermal related properties (see Figure 16). The mesh spatial resolution and programming language differs for each software; therefore, an intermediate layer is needed for transferring the density and energy deposition quantities between both software's.

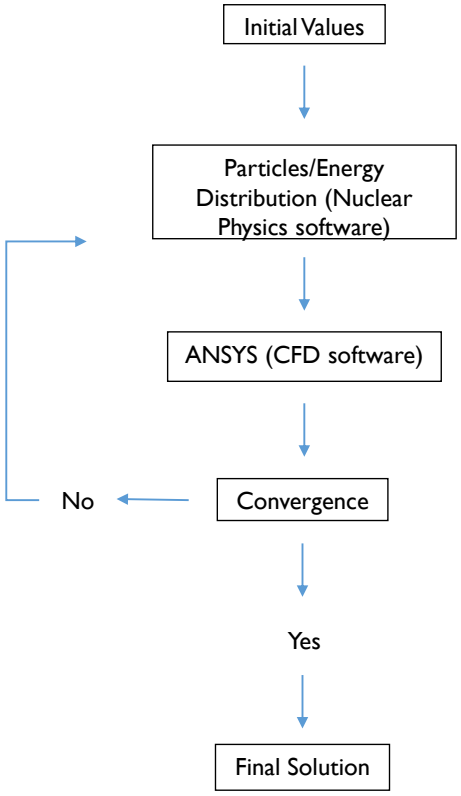

Figure 16 - Schematic figure of the coupling approach between ANSYS and an external Nuclear Physics software.

Grahn, A. developed an analysis of a nuclear reactor safety based on the coupling between the reactor dynamics code DYN3D and ANSYS-CFX (43). DYN3D was used to calculate the neutron kinetics and the heat transfer from the fuel to the coolant. The coupling with ANSYS-CFX was made since this software provides an optimized three-dimensional coolant temperature distribution. A comparison between the DYN3D stand-alone and the coupling approach revealed that the temperature and density distributions on both results are congruent. This result validates the ANSYS-CFX as a CFD analysis tool to study the targetry thermal performance.

Faugl et.al developed a model implementing the iterative coupling between ANSYS-CFX and the Monte Carlo radiation transport software MCNPX (44). Combining thermal and fluid modelling with the accurate proton energy deposition on liquid target, the main objective was to study how the beam range varies when compared with the static volumetric heat deposition. Achievable solution times were obtained by applying local mesh refinement methods and to decouple the cooling water, until the density distribution reached

convergence. This work allowed to conclude that, once considering the non-uniform density distribution, the beam penetrates further in the target and the Bragg peak presents a broader region of energies.

A recent work from a s two-way Multiphysics coupling was made to model the Rubidium chloride (RbCl) production target (45). The energy deposition was calculated using Monte Carlo N-Particle code (MNCP) and, in its turn, ANSYS-CFX was used to calculate the density and temperature distributions, as well as the heat deposition. Considering that the input and output data formats are different for MNCP and ANSYS-CFX, there was the necessity to translate the data. In order to do this, MATLAB was used to translate ANSYS density spatial distribution and the energy deposition profile from MNCP. The process proved to be time-consuming, taking three months of simulation time even when using an Intel processor with ten cores. Progressive phase change and the transient behaviour of the cooling water was fully resolved choosing a step size of 0,25 ms. The thermal results allowed to calculate the temperature, velocity and liquid fraction values for all the target domains. Hence, it was possible to demonstrate that the coupling approach is capable of successfully modelling a problem with this scale and high complexity. However, the authors concluded that the model accuracy could still be improved by adding a model for the boiling near the wall. This proved that the implementation of the phase change process and the coupling with an external nuclear physics software and a thermal analysis is possible and accurate; although vast computational capacity is mandatory.

Simulation Model Validation

As stated before, there is almost no experimental data regarding the Nirta C8® liquid target. The simulation model could only be considered representative of the liquid target thermal performance, once validated with experimental results. do Carmo *et al*. (46) measured the cooling water temperature for the Niobium Nirta C8® target under distinct irradiation conditions. The implemented monitoring system can be used as a comparison tool, in order to validate the CFD simulation model carried out on this thesis. Thermistors were implemented at the back of the niobium insert (inlet), at the exits of the target (outlet) and collimator water cooling channels to enable measurement of the temperature of the cooling water right before entering the target (inlet), immediately after its interaction with the target system (outlet) and then after exiting the collimator. The authors concluded that the temperature of the refrigerated

water increased linearly with the proton current, about 1ºC for each 10μA increment. It was also verified that significant variations of the inlet cooling water temperature almost do not influence the temperature increment in the cooling water. The simulation outputs will be compared with the obtained results in this work.

Objectives

All the previous studies support the suitable use of ANSYS-CFX software to develop a model capable of simulating the liquid target thermal performance. CFX will allow to study the coolants effect on the system, as well as the temperature distribution as a function of the proton beam current, and to implement the proton energy deposition previously calculated on a particle physics software.

The main objective of the present work was to develop and validate a model capable of simulating the thermodynamic behaviour of the liquid target system previously described. The niobium window implemented on the ^{68}Ga production through the irradiation of liquid targets presents a considerable thickness. Consequently, the heat generated at the window is significant. Therefore, the 250μm niobium window was chosen for the simulation. The liquid target was assumed to be liquid water. At first, the aim was to calculate the beam energy deposition using the SRIM software and implement the consequent generated power on both the target window and liquid target accordingly. It is expected that temperatures inside the liquid target reach its maximum on the location near the window since the latter heats significantly. It is also expected that the liquid target temperature increases with the target depth, considering that the Bethe-Bloch formula dictates the energy deposited per volume. Another objective was to validate the simulation model by comparing the calculated temperatures with experimental results obtained on the He cooling water system (46). One more goal consists was to study the simulation sensitivity to the cooling water and helium initial conditions, by considering for both cases the inlet temperatures and mass flow rates.

Once the simulation is validated, it will allow to study the mechanisms involved in the liquid target. Therefore, a simulation model that allows to study the target thermal

performance, will enable discovering alternatives to increase the proton current reaching the liquid target.

Chapter II. Methods and Simulations

Initially, all the components of the liquid target system were designed and divided in finite elements to apply the governing equations. Once the structure was defined, CFX-Pre was used to implement the initial and boundary conditions and the mathematical models representing the thermal behaviour of the target system. Then, in order to simulate the profile of the proton's energy deposition, SRIM software was used to calculate the energy lost profile by ionization in the window and in the liquid target. These data were posteriorly converted into deployed power in these domains in ANSYS-CFX software. The simulations were calculated in an iteration step process until convergence was achieved. Lastly, CFX-Post provided a 3D and graphical interface to observe the variables of interest, namely the temperature and density distribution.

Fluid Dynamic and Physical Models Implementation – ANSYS CFX

Geometry Definition

The first step of simulation was to define the geometry and design of the solid and fluid domains composing the liquid target system represented in the simulation. The geometric components (see Figure 6 and Figure 17) were designed using the 3D design software Inventor (Autodesk, Inc., 2019) After designing the simulation components, the geometry is discretized in finite elements in a process known as mesh.

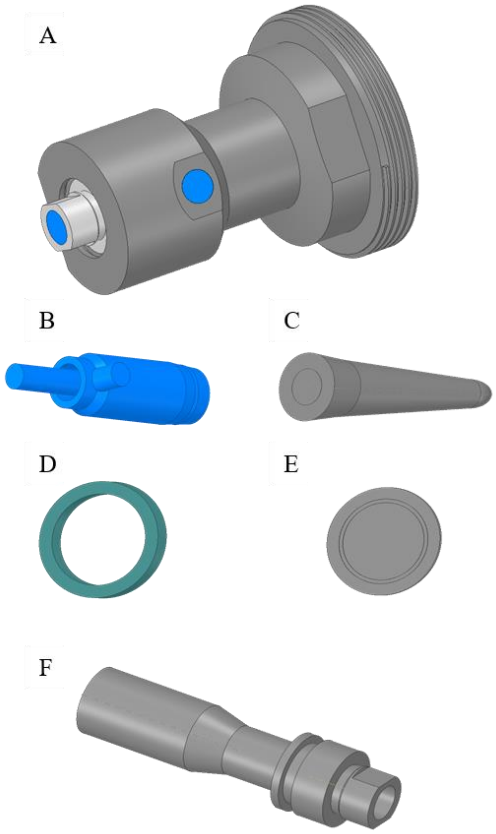

Figure 17 - Simulation Solid and Fluid Domains: A) - Target Support; B) - Water Cooling domain; C) -Liquid target Domain; D) - O-Ring; E) – Target Window, F) - Diffuser.

Mesh Definition

The quality of the mesh is crucial for the stability and accuracy of the numerical computation and can be evaluated by three average properties: *skewness*, *orthogonal quality* and *aspect ratio*.

Skewness refers to how close the cell shape is to an equilateral, which is considered the ideal cell size. *Orthogonal quality* measures how close the angles between adjacent elements are to the ideal ones. Finally, *aspect ratio* considers the degree of how an element is stretched. The optimal skewness is achieved at 0 while optimal orthogonal quality corresponds to 1. Aspect ratios below 100 are acceptable. When combining these properties, the computational model accuracy is directly proportional to the number of nodes and elements (47). However, when the number of elements is large, the computational effort and the calculation time also increase. It is important to acknowledge that a higher quality mesh can be extremely time-consuming. Considering that an optimized mesh could imply several days of simulation for each run and that, on the other hand, a simplified mesh could lead to inaccurate results.

Considering the limited memory and processing capacities of the personal computer used, and also that the aimed simulation is complex, the only suitable approach to study all models involved was the use of a less demanding mesh (see Table 2) through the work. However, in order to study the influence of the mesh quality on the simulation results, one simulation run was executed with a fine mesh, i.e. with a larger number of nodes and elements (see Table 3). Tetrahedron elements of quadratic order were used for both meshes.

Table 2 - Mesh quality parameters and correspondent standard deviation, used in the less demanding mesh.

Number of Elements	290293
Number of Nodes	589535
Average Skewness ± Standard deviation	0,287 ± 0,213
Average Orthogonal Quality ± Standard deviation	0,705 ± 0,216
Average Aspect Ratio± Standard deviation	9,155 ± 16,003

Accordingly, the geometry domains were discretized in thousands of elements (Figure 18).

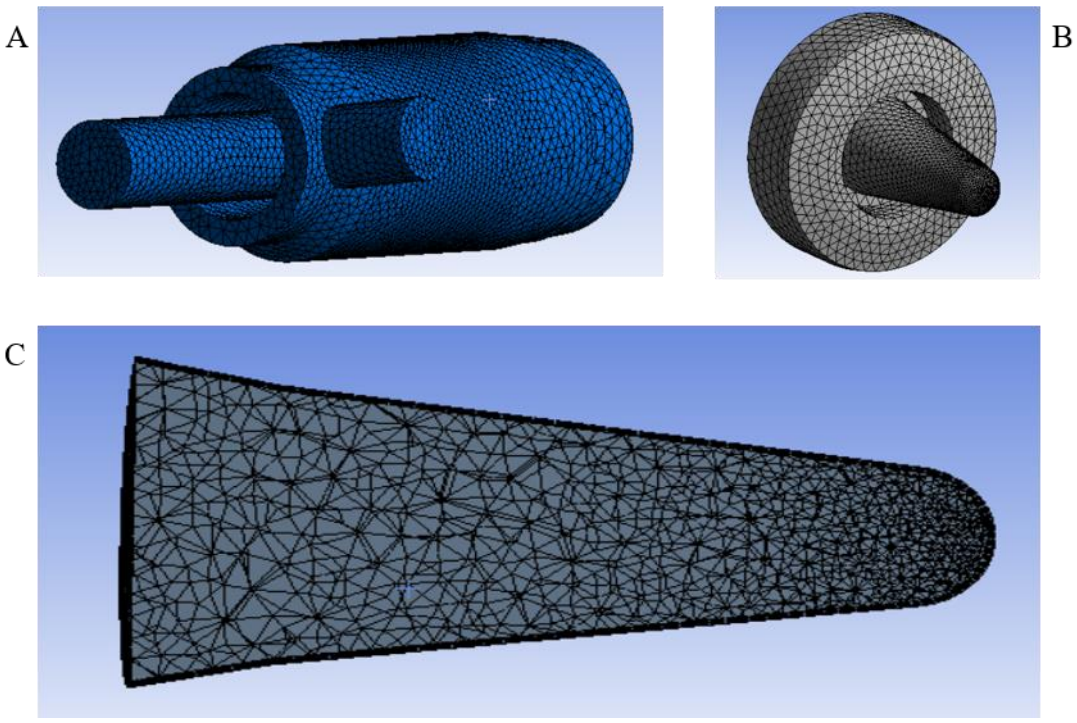

Figure 18 - Domain meshes used: A) cooling water domain mesh; B) conical target domain mesh, C) liquid target domain mesh.

Given that the computational effort increases for a larger number of elements, it is prudent to use local refinement, ensuring that critical areas present a finer mesh. Considering

that the heat is generated on the window and liquid target, variations will be significant on these domains. Also, when compared with the latter, the temperature variations on the remaining target diffuser and support, do not justify the mesh improvement. Thus, the mesh was improved for the beam energy deposition area (see Figure 19) resulting in the following parameters (Table 3).

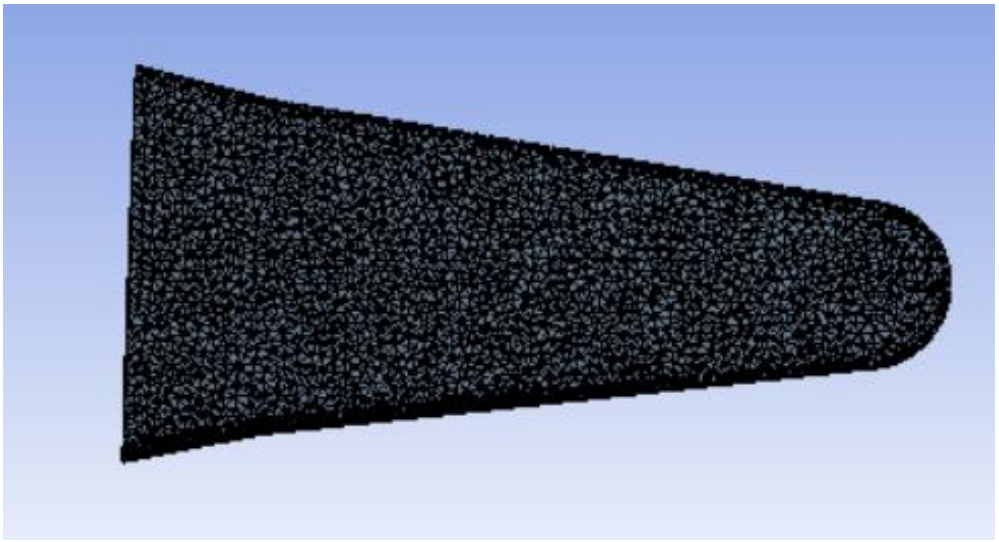

Figure 19 - Liquid Target domain using a finer mesh.

Table 3 - Mesh quality parameters and correspondent standard deviation, for the finer mesh.

Number of Elements	458201
Number of Nodes	871298
Average Skewness ± Standard deviation	0,268 ± 0,190
Average Orthogonal Quality ± Standard deviation	0,725 ± 0,192
Average Aspect Ratio± Standard deviation	6,881 ± 12,99

Comparing the mesh properties from tables 2 and 3, one can conclude that the quality of the mesh was improved. Results comparing the implementation of these meshes will be presented on the following subchapters.

Heat transfer from the fluid to the solid takes place at the domain boundaries; therefore, it is advisable to improve the mesh on the fluid domain boundary to accurately simulate the heat transferred to the adjacent solid. This process is known as inflation (see Figure 20) and was implemented on both the cooling water and liquid target domains.

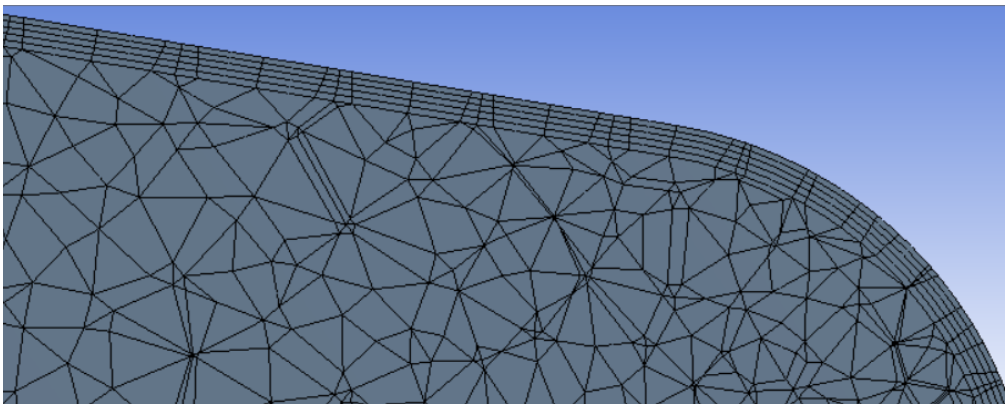

Figure 20 - Inflation layers for the liquid target domain.

In the next chapters the influence of the mesh on the simulation model will be tested, using both meshes previously described (tables 2 and 3).

Pre-Processor

In this pre-processor, the mesh configuration is imported, and all the physical models related to momentum and energy are defined, as well as the initial and boundary conditions of the simulation.

Fluid Domains

Liquid Target Domain

A typical liquid target is partially filled with water, while the remaining volume is occupied with air at atmospheric pressure. As the conical insert is continuously cooled by the cooling water flow, temperatures on the liquid target boundaries are inferior, leading to the condensation of the previously formed steam. However, the presence of air and the implementation of the phase change associated with water and steam, would increase the complexity and computational time of the simulation. Hence on these simulations, it is assumed that the conical insert is filled only with liquid target. The absence of the gaseous states would lead to an untruthful pressure value calculated on the simulation. As a consequence, the pressure developed inside the conical insert will be considered constant and equal to the atmospheric pressure.

The material chosen for the liquid target was: pure water substance with constant density 997 kg/m^3 and specific heat capacity at constant pressure of 4181,7 J/kg K. Turbulence is modelled by the k-ε model and gravity and density difference effects are considered trough

buoyancy. Initial conditions assure that the water starts at the atmospheric pressure and at a temperature of 23°C.

Cooling Water Domain

Contrary to the liquid target which is confined to the cavity of the conical insert, the cooling water flow enters at the back part of the target (inlet), flows between the conical target and the diffuser and posteriorly between the diffuser and the support till it ends at the side of the support (outlet) (see Figure 6).

At first, the cooling water material was defined with temperature dependent density and specific heat capacity (48). It was observed that although the inlet initial temperature was 23ºC, the temperature of the cooling water in contact with the lateral surface of the rear part of the conical insert, decreased to almost 0ºC (Figure 21). This result is a calculation error since the heat goes from the conical insert to the cooling water and, consequently, the cooling water temperature increases near the niobium surface. Therefore, the cooling water material was replaced with water with constant thermodynamic properties. The discrepancy previously observed was no longer detected. Instead, the water-cooling temperature increased near the conical insert, due to the heat transfer from the latter to the coolant (see Figure 22). Since the temperatures of the cooling water present no significant variations, it is acceptable to assume a constant density.

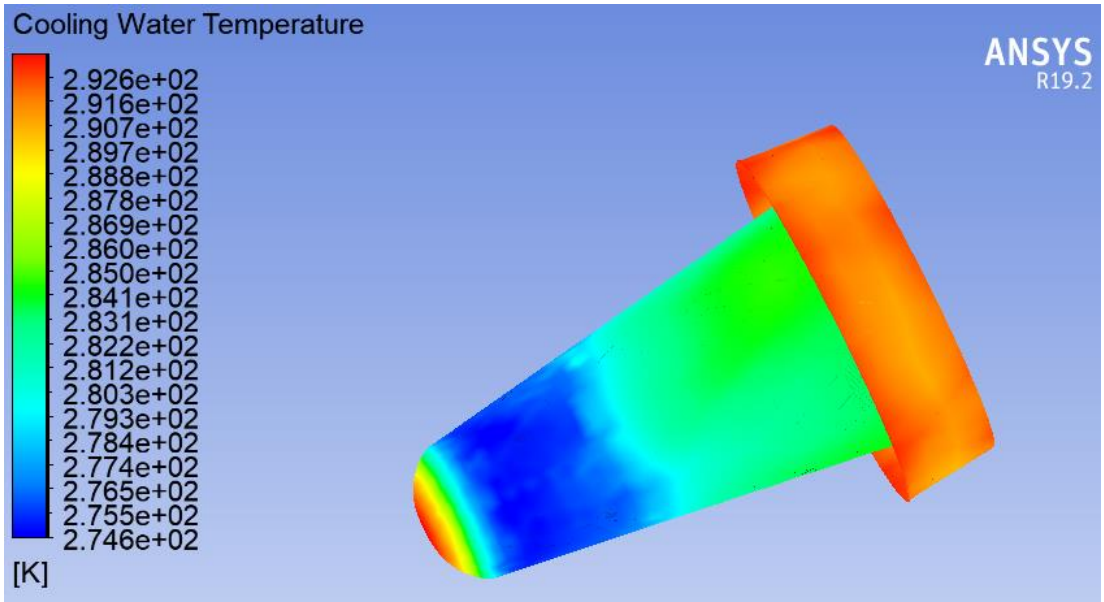

Figure 21 - Cooling water temperature near the conical insert surface for a water material with temperature dependent thermodynamic properties.

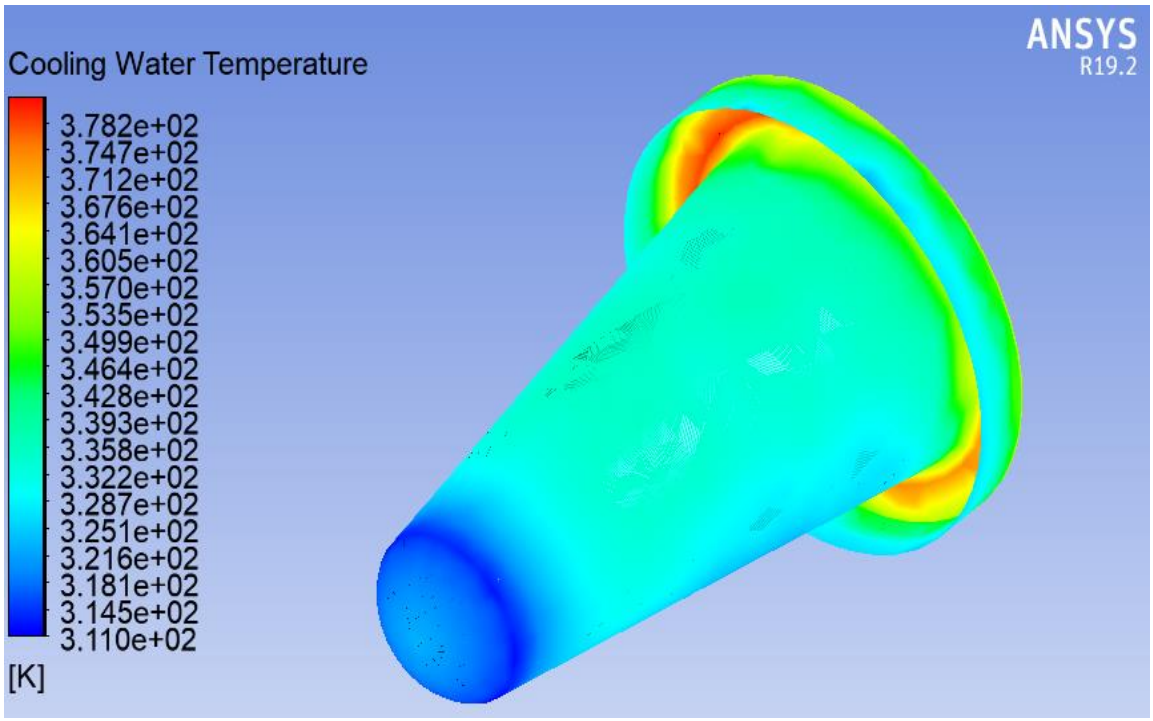

Figure 22 - Cooling water temperature near the conical insert surface for a water material with constant thermodynamic properties.

The water material chosen for the cooling water was the same as for the liquid target (constant properties). Both inlet and outlet configurations are settled as boundary conditions: inlet temperature and mass flow rate of 23°C and 3kg/min respectively. The latter is equivalent to the mass flow rate reaching the liquid target in the cyclotron and is conserved trough the cooling water path. For the cooling water the aim is to study the heat transferred at the boundaries of the conical insert/cooling water surface. Due to the SST model higher accuracy in the modelling of the fluid boundaries, it was the selected model for describing the turbulence effects of the cooling water.

Solid Domains

The solid domains of the target system are composed by the niobium window and conical insert, the aluminum diffuser and support, and the Viton O-Ring (see Figure 6). The initial temperature for all the solid domains is 23ºC and all the thermodynamic properties of the solid materials were considered temperature independent at first. In a typical cyclotron bombardment, the window is cooled by gaseous helium on the side opposite to the conical insert.

Various tests were performed with the purpose to verify that the basic physic mechanisms were working properly, such as the heat transfer between fluids and solids. In order to verify these, an isolated closed niobium cube with 2 mm thickness, was designed and completely filled with liquid target. The heat was generated through an energy source of 1000 W equally distributed in all the fluid domain. The initial temperature difference between niobium and water was set as 100 K. The evolution of both water and niobium temperatures was tracked, with the purpose to verify whether the thermodynamic equilibrium was achieved, which was confirmed.

The heat transfer is characterized by the thermal energy model accounting for the enthalpy/temperature equation granting energy conservation. To enable heat transfer between attached fluid and solid domains, interfaces were defined with the coincident surfaces of both domains. Conservative interface flux guarantees the heat flux conservation and general grid interface (GGI) ensures the connection of surfaces even if they do not present aligned grid nodes

Heat Transfer Coefficient

The heat transfer of the liquid target system to the surrounding air and cooling helium, can be modelled by a boundary condition with a certain heat transfer coefficient. Thus, this eliminates the necessity to include the physical presence of both these fluids, and consequently, reduces the computational time of simulations. Namely for the cooling helium, the h_c is equivalent to the gas mass flow rate, flowing near the target window.

As previously mentioned, the heat transferred between the fluid and a surface with different temperature is proportional to the heat transfer coefficient value. It is therefore mandatory to accurately define the h_c which represents the real value. There are multiple correlations in order to calculate the h_c depending on the nature of the flow, that is, if the flow is laminar or turbulent, and also for the natural or forced convection.

The target system geometry is surrounded by air, more specifically, air is in contact with the outer surface of the target support and one part of the diffuser, which present an approximated cylindrical shape. This way, the convection induced by the surrounding air can be classified as natural convection around a long horizontal cylinder. (49), where the Nusselt number can be estimated by:

$$\mathrm{Nu} = \left[0{,}6 + \frac{0{,}387\ (GrPr)^{\frac{1}{6}}}{\left[1+\left(\frac{0.559}{Pr}\right)^{\frac{9}{16}}\right]^{\frac{8}{27}}} \right]^2 \quad [24]$$

It is assumed that cooling helium flows parallel to the target window, therefore it can be seen as forced convection for flow parallel to a flat plate. The Reynolds number for the flow parallel to flat plate, $\mathrm{Re_L}$ is defines as:

$$\mathrm{Re_L} = \frac{v\,L\,\rho}{\mu} \quad [25]$$

where v is the fluid approach velocity, L the length of the plate, ρ the fluid density and μ the dynamic viscosity.

For values of Re_L inferior to 200000, the boundary layer of the flow is considered laminar where Nu is defined as (50):

$$\mathrm{Nu} = 0{,}664 \times \mathrm{ReL}^{\frac{1}{2}} \times Pr^{\frac{1}{3}} \quad [26].$$

Finally, the heat transfer coefficient can be calculated by replacing Nu values on equation 13.

It was considered that air and helium presented a temperature of 20 ºC. Thus, boundary conditions were defined with an outside temperature of 20 ºC and heat transfer coefficients of 17 W/m^2 K for the diffuser, 7 W/m^2 K for the target support, and 50 W/m^2 K for helium.

Solver

It is possible to control the interpolation, memory usage, precision, convergence and detailed flow and physic properties calculation. These can be controlled by the coefficient loops, residuals, advection and transient scheme, executables and expert parameters. To control the solver operation, the selected advection and turbulence numerics were high-resolution. Also, the selected transient scheme was the second-order backward Euler. For the convergence control, 8 coefficient loops per iteration were defined and the converge criteria was established at the RMS residual value of 1×10^{-6}. The time step selected for the simulations was 0,25s with a total simulation time of 120s, which is equivalent to 480 iterations.

Executables (files containing computer programs) are responsible for the partitioning and interpolation capabilities. For the solver initialization, two executers were adjusted. Double precision store floating points number as 64-bit words and is responsible for greater accuracy in numerical operations, although it consumes more memory. In its turn, memory allocated factor, which controls the memory used by the solver, is defined as the maximum possible value.

Implementation of the Beam Energy Deposition – SRIM and ANSYS CFX

In order to calculate the protons energy loss, the SRIM software was used. Particles with 1,00727 amu (proton mass) and 18 MeV, with an angle of incidence of 0º with respect to the target window, were used as incident particles in two layers (Figure 23).

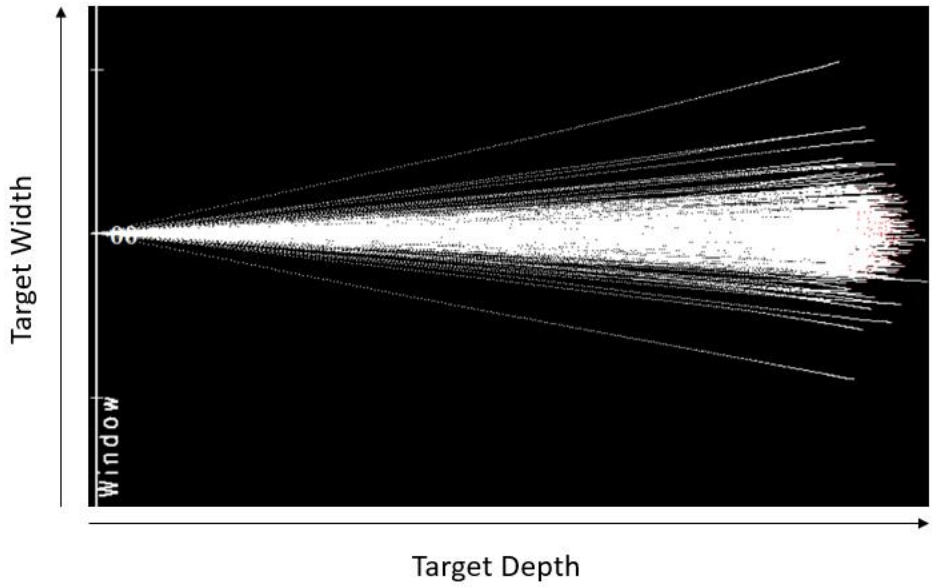

Figure 23 - Proton paths on the window and liquid target, calculated on SRIM.

Titanium window was not considered for calculations. The first layer is pure niobium with a thickness of 250 μm (window) and a density of 857 kg/m^3. The window is responsible for an energy loss of 3,7 MeV, resulting in remaining 14,3 MeV protons impinging

on the second layer. The second layer is the liquid target made of the water/steam mixture with a density of 69,23 kg/m^3. This density was chosen so that the Bragg peak and, consequently, the protons maximum range is positioned exactly at the end of the target insert. For a typical ^{18}F liquid target irradiation, the target is normally filled with 81% water (ρ = 998 kg/m^3) and the remaining 19% with air (ρ = 1,29 kg/m^3). Since the mass and volume are conserved, the average density inside the conical target is constant and approximately 809,43 kg/m^3. Comparing with the value used on SRIM for the second layer, i.e. 69,23 kg/m^3, it is noticeable that the density variation on the beam area, due to the generated heat, is significant. This can be explained by the presence of steam resulting from the water evaporation.

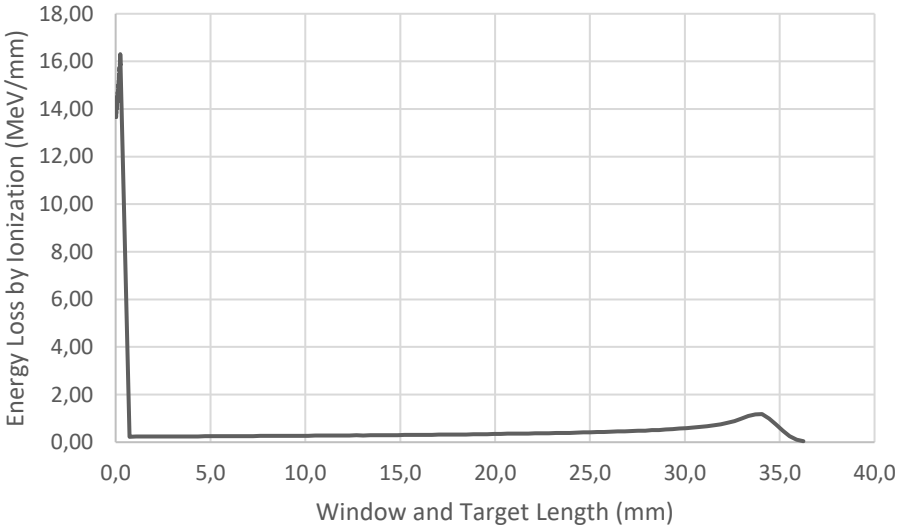

Figure 24 - Stopping-power at the target window and water calculated by SRIM.

The calculated energy deposition was then implemented on ANSYS-CFX, testing different approaches. For the target window, the energy deposition was defined by an energy source whose dimensions were delimited by a function, resulting in a cylinder with a diameter of 9,5 mm (collimated beam), covering the entire window length. This way, the generated power resulting from the energy loss in the window, corresponding to 3,7 MeV, was equally distributed along its cylinder "subdomain".

In its turn, the heat deposition on the liquid target was implemented with four different approaches:

i) At first, the beam power was equally distributed through the entire target fluid domain. A source of power geometrically delimited by the fluid domain was defined. It was

verified that the temperature of the liquid target increased equally, except for the locations near the conical insert surface due to the cooling water effect. This result allowed to validate the use of the energy source to replicate the beam in a more truthful method.

ii) Since the collimated beam admits a diameter of 9,5mm, a good approximation of the beam profile is to define the power generated through cylindrical domains. Another more accurate approach consisted in distributing the power in cylindrical subdomains inserted on the fluid domain, previously designed on Space Claim. At first, the power was divided in two long cylinders with 9,5m of diameter centred and covering almost the entire target range. The implementation of 2 cylinders allowed to confirm that it was possible to equally distribute the deployed power in a multiple number of subdomains. This resulted in an increase of temperature of the water in the cylinder's region when compared with the rest of the water, proving that the heat is being generated accordingly with the cylinder reference location.

iii) Posteriorly, the heat generated along the fluid was divided into 8 cylinders in order to replicate, more accurately, the energy deposition calculated in SRIM and consequently, the Bragg peak effect. This way, the energy of each cylinder was assigned considering the average energy deposition calculated for layer 2 on SRIM (Figure 24). Contrary to the previous approaches, the energy is no longer equally distributed along the target in this configuration, as expected and pretended, resulting thus in a better approximation of the true energy profile, since most energy is deposited in the window and at the end of the path (Bragg peak). The cylinder's length and diameter vary for every cylinder. Starting from the window, the first two cylinders present a 9,5 mm diameter and the remaining cylinder's diameters was adjusted to remain inside the liquid target. As can be seen in figure 23, the beam tends to disperse as it travels through the liquid target. Thus, the cylinders diameter reduction with the target depth does not correspond to the real beam dispersion. This approach was made in order to obtain an easier implementation of the power generated by the beam in the liquid target.

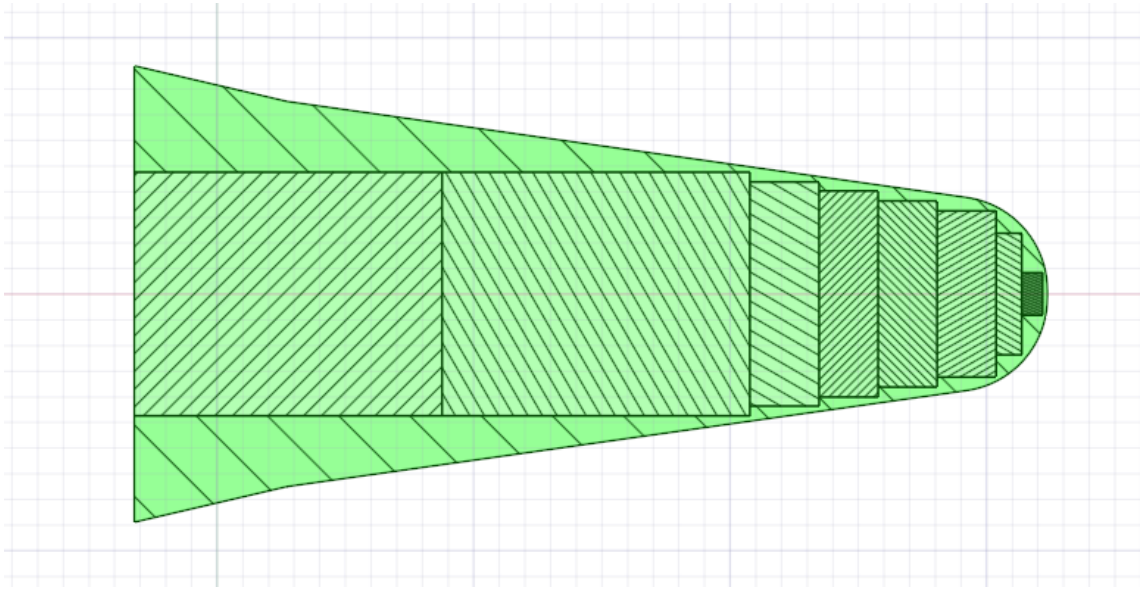

Figure 25 - Cylinder geometric domains used as a reference to the energy sources inside the liquid target.

When comparing the liquid target average temperature obtained with the 2 and 8 cylinders configurations, it was observed that, the mean temperature was about 100 K below in the latter. This difference is much higher than expected due to the non-uniform energy distribution. Thus, a test with an improved mesh was done for the 8 cylinders' approach in order to investigate the source of discrepancy. The resulting average water temperature was similar to the 2 cylinders' approach, which indicated that the problem arose from the limits between the cylinders themselves. Mass and energy conservation are ensured by the conjugate heat transfer and the mesh compatibility between different surfaces is also assured by the use of GGI (General Grid Interface). However, this demonstrated that it was necessary to implement a finer mesh to accurately calculate the temperature distributions. However, such finer mesh increased the computational time from 10 to 70 hours, which showed that using previously designed cylinders to deploy the protons energy, following the Bethe-Bloch formulation, is impracticable. Therefore, a fourth approach was implemented.

iv) Instead of using geometric subdomains, functions were used to delimit the cylinder's dimensions and define the energy source location. This away, the power deployed continues to follow the SRIM calculated energy deposition (Figure 26) and simultaneously avoids the necessity of a finer mesh; assuring an accurate temperature distribution and time-effective simulation. The average liquid target temperature was approximately close to the 2 cylinders' approach, which supports the validation of this method. It was verified that the

temperature increased trough the liquid target domain, following the beam profile, opposing the equally distributed temperatures for the equally generated power approach (i).

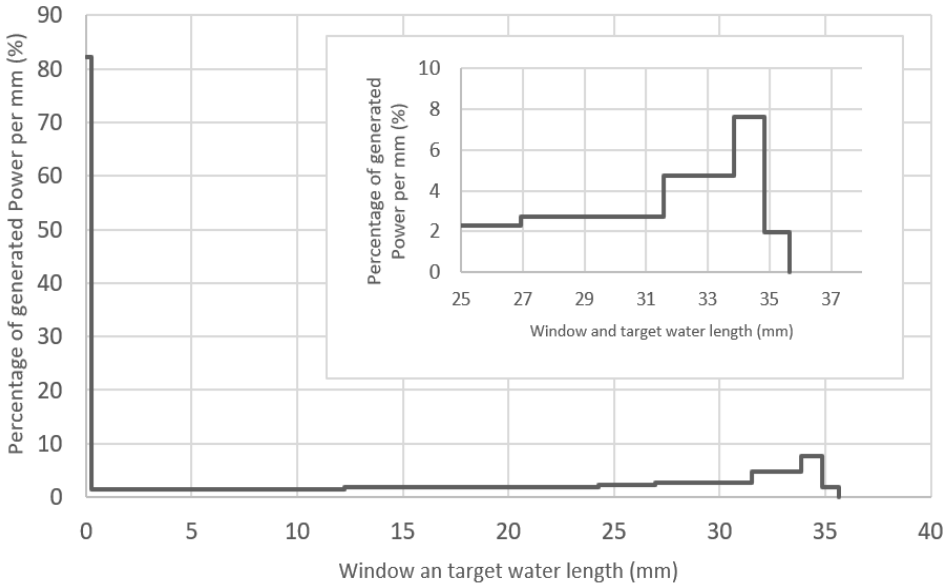

Figure 26 - Percentage of generated power at the target window and water implemented on ANSYS-CFX.

Comparing figures 24 and 26, the profile of the power deployed on the target window and liquid target on ANSYS-CFX, replicates the proton´s energy lost by ionization calculated on SRIM, assuring that the energy deposited by the proton current is correctly implemented on the simulation. Due to the fact that most of the energy is deposited in the window and at the end of the target (Bragg peak), it is then expected that the temperatures observed on these locations are the highest registered.

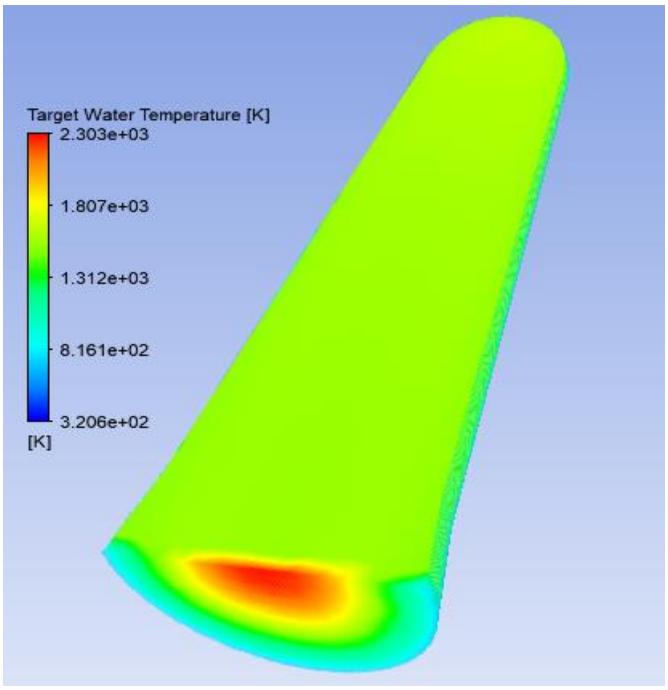

Figure 27 – Temperature distribution inside the target.

Looking at Figure 27, one might incorrectly perceive that the liquid target temperature is uniform throughout the volume (due to the large scale), except for the area near the window, where the temperature reaches its maximum (in red). This arises from the fact that the liquid target maximum temperature is much larger than the average registered temperature. This may mislead and indicate a uniform heat generation throughout the liquid target volume. Figure 28 represents the liquid target temperature where the temperature range was adapted in order to focus on the effect on the temperature distribution, of the implementation of the energy deposited calculated on SRIM. Notice that the temperature range does not match the real values distribution, it is only for visualization purposes. It is then possible to observe, that the liquid target temperature increases when approaching the rear part of the target. This is congruent with the fact that the energy deposited per unit of area increases with the penetration range and reaches its maximum, at the Bragg peak, positioned at the end of the target.

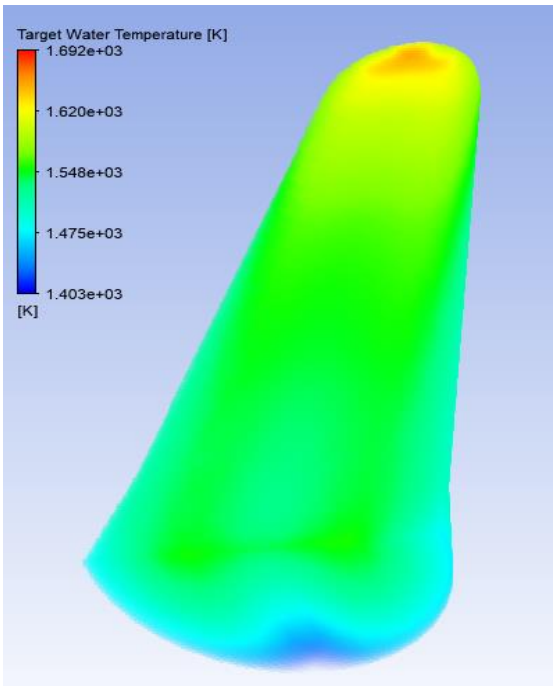

Figure 28 – Temperature distribution inside the liquid target, with temperature scale adapted to observe the proton energy deposition implementation.

Figure 29 shows the temperature distribution on the niobium window, due to the beam generated heat. The collimated beam presents a diameter of 9,5mm, therefore, it is expected that the temperatures reach its maximum on the centre of the window, as can be observed. The obtained results demonstrated that the temperatures are higher on the surface of the window next to the liquid target. This is agreement with the helium cooling effect on the other side of the window.

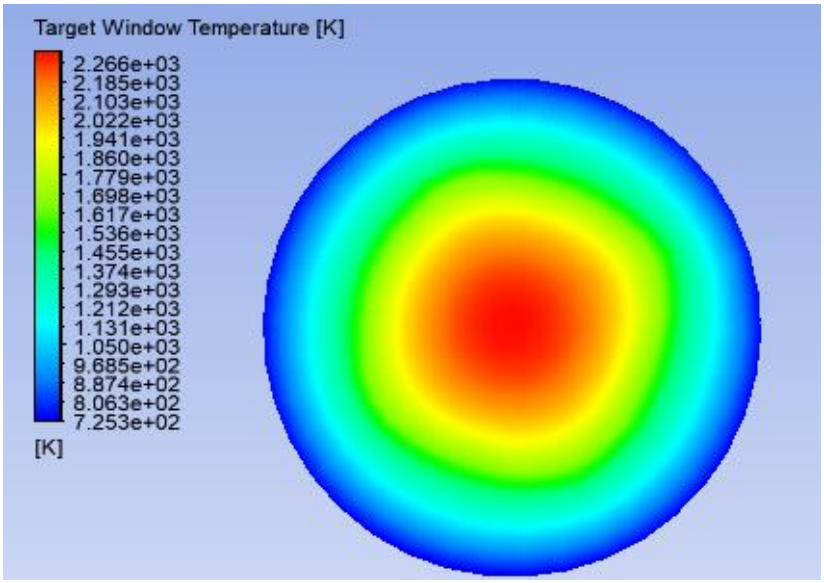

Figure 29 - Target window temperature for a deployed power of 1000W.

It was verified that the temperature of the conical insert increased though its domain and especially on the location near the window (see Figure 30). This result corroborates the heat transfer from the window and liquid target to the conical insert.

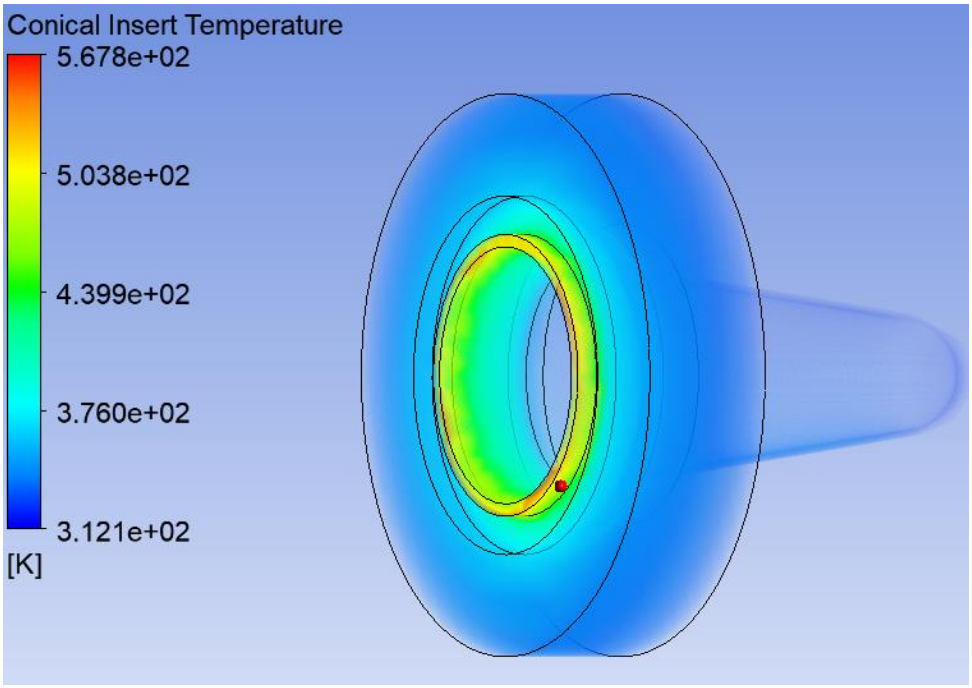

Figure 30 - Conical insert temperatures for a deployed power of 1000W.

Model Validation

Timestep and Mesh Independence Study

CFD simulations can be strongly influenced by the time step and mesh. Thus, in order to evaluate the influence on the simulation of these two simulation properties, two simulation runs were made, one with ten times smaller time step, i.e. 0,025s, and one with a finer mesh, where the number of elements was increased on the window and liquid target (referred on the mesh chapter). Average temperature values of the different domains were compared, and it was possible to conclude that the time step of 0,25 was in complete agreement with this simulation, since temperatures of both simulations were practically the same. On the other hand, it was verified that the average temperatures of the target window and liquid target in the simulation with a finer mesh (table 3), were similar to those of the initial mesh (table 2).

Considering that a better-quality mesh increased the computational time of the simulation from 10 hours to about 70 hours and knowing that the temperature difference is small when compared with the average temperature values of thousands of degrees Celsius, it is not advantageous to use the finer mesh. Hence, all the simulations will be carried out with 290293 elements and 589535 nodes.

Considering the previous preliminary tests and calculations, the reference parameters for the following simulations are displayed on table 4.

Table 4 - Reference simulation parameters.

Cooling Water Mass Flow Rate (kg/min)	Cooling Water Temperature (°C)	He h_c (W/m2 K)	He Temperature (°C)	Mesh	Timestep (s)
3	23	50	20	Table 2	0,25

Cooling Water Temperature vs Target Current

The power deposited by the proton current in the target is proportional to the target current (see Equation 18). The resultant heat will be transferred to the cooling helium and cooling water by convection, as previously explained in chapter 1. Thus, the cooling water temperature will vary accordingly with the target current.

With the purpose to compare the simulation results with the temperature monitoring study (46), the temperature of the cooling water and other target components was observed for different values of deployed power correspondent to the respective target current values. To fully obtain the convergence of the system, simulation runs with a time step of 0,25s, totalizing a simulation time of 120s, were made. The convergence can be confirmed observing both figures 31 and 32, where the system variables stabilize, and the residuals reach a low value between 1×10^{-5} and 1×10^{-6}. For every simulation realized for the present work, the convergence of both the residuals associated with the solver and the stabilization of the system variables, is ensured, relying on similar graphics.

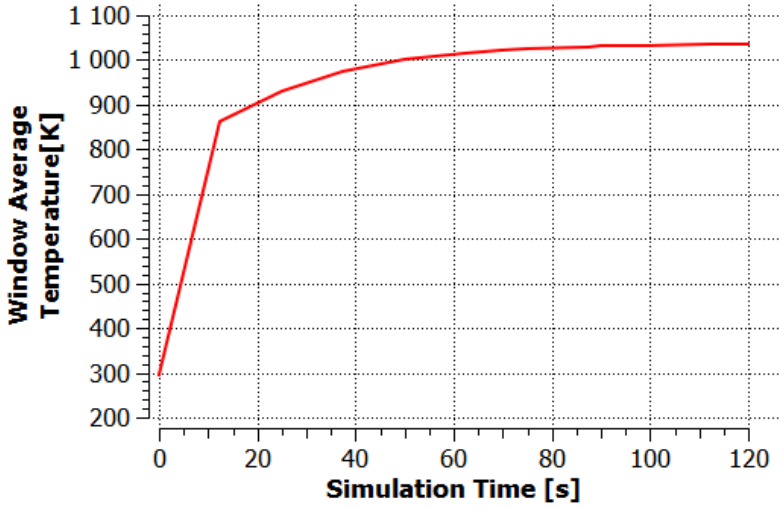

Figure 31 - Window average temperature value stabilization.

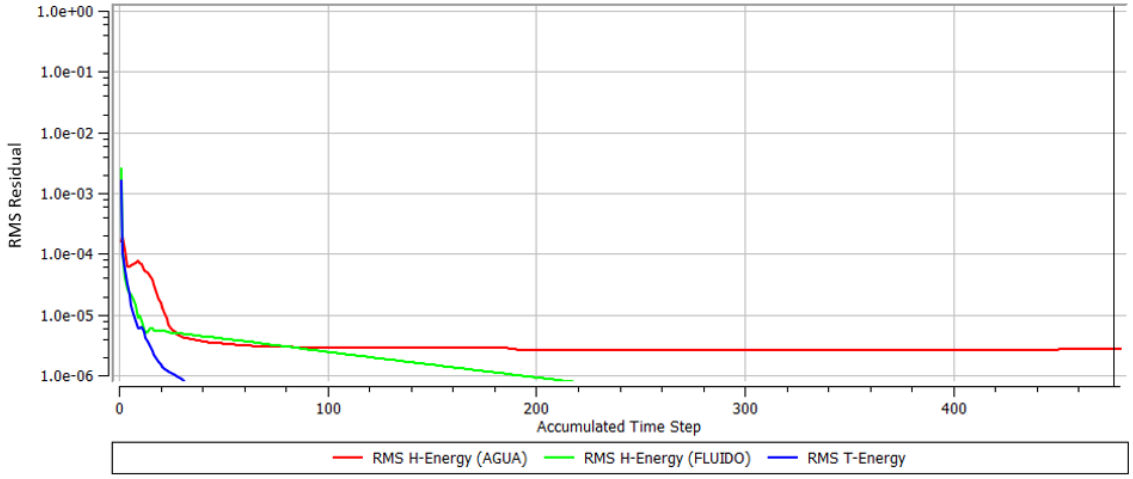

Figure 32 - Heat transfer RMS (Root Mean Square) residuals.

Table 5 presents the temperatures of the liquid target, target window, cooling water and conical insert, for the equivalent proton current. The power deposited by the beam corresponding to a certain proton current was also presented (see equation 18). Figure 33 represents the temperature increments (related to 23 ºC) for a clear perception of the temperature dependence with the target current.

Table 5 - Temperatures of conical insert, liquid target, window and cooling water the several proton currents and equivalent deployed powers.

		Conical Insert			**Liquid target**			**Window**			**Cooling Water**		
Power (W)	**Proton Current (μA)**	Av. T (°C)	T_{max} (°C)	ΔAv. T (°C)	Av. T (°C)	T_{max} (°C)	ΔAv. T (°C)	Av. T (°C)	T_{max} (°C)	ΔT_{max}(°C)	Av. T (°C)	Outlet T (°C)	ΔOutlet T (°C)
250	**14**	37	91	14	429	659	406	232	665	642	23.89	24.13	1.13
500	**28**	50	158	27	739	1250	716	427	1260	1237	24.80	25.28	2.28
1000	**56**	77	285	54	1279	2369	1256	798	2389	2366	26.62	27.61	4.61
1500	**83**	103	408	80	1761	3433	1738	1152	3461	3438	28.46	28.94	5.94
2000	**111**	129	530	106	2205	4460	2182	1495	4497	4474	30.30	32.27	9.27

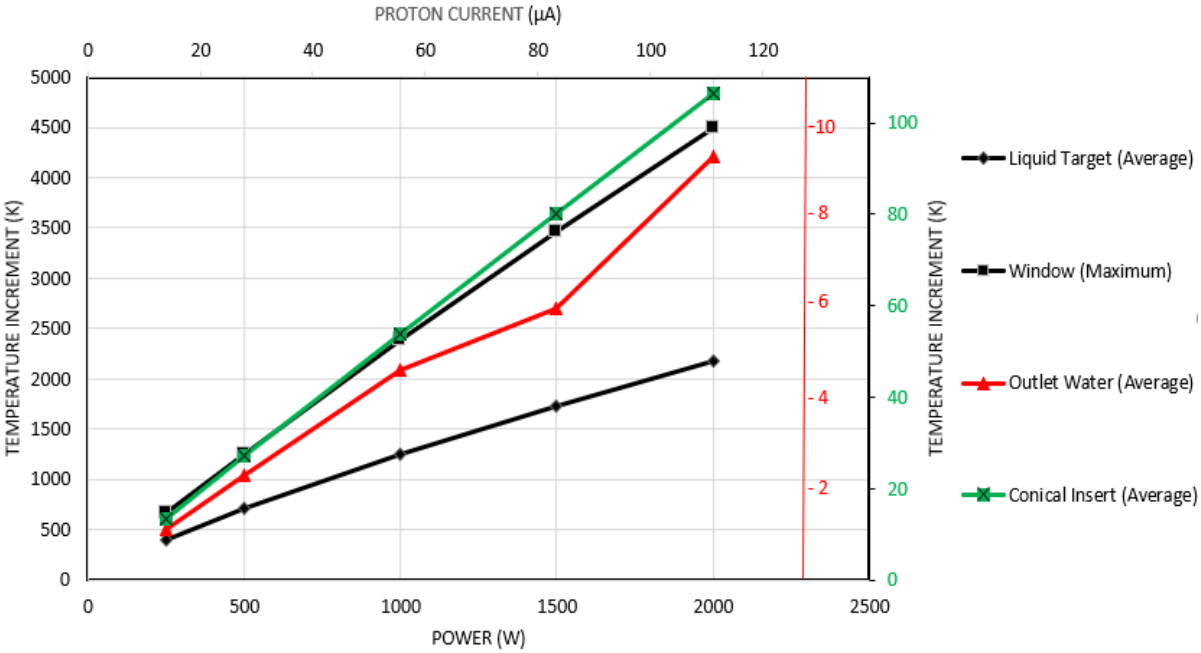

Figure 33 - Average temperature increments for the liquid target, outlet water and conical insert and maximum temperature increment of the window, for different values of the proton current and correspondent total deployed power. All increments are related to the initial temperature of 296,15K.

The maximum temperature of the niobium window presents a higher relevance for thermal analysis, when compared with its average temperature. Thus, it was the chosen variable for graphical representation and to deduce conclusions.

When analyzing Figure 33, it is clear that the temperature of all the different components of the target system increases linearly with the heat generated by the beam. The most important result is the linear increment of the temperature of the outlet cooling water with the target current. Comparing with the results from (46), it was also verified that the average increment of the outlet water temperature, increases with the same proportionality with the target current. Thus, it can be considered that the simulation results are in congruence with the measured temperatures.

In a typical irradiation for the production of ^{68}Ga, the maximum proton current reaching the target is about 65 μA, which corresponds to a maximum deployed power of 1170 W. On table 6 it is possible to see that for a power of 1000W, the maximum verified window temperature is 2366ºC (see Figure 29). Considering that the melting point of niobium is 2477ºC it is possible to conclude that in order to increase the proton current reaching the target it is mandatory to improve the window helium cooling. Another conclusion can be that the helium boundary condition, i.e. the helium heat transfer coefficient, calculated is smaller than the real

value. It is then important to study the influence of different h_c values associated with the convection heat transfer imposed by helium.

Niobium Thermodynamic Properties Temperature Dependence

The niobium temperature increases accordingly with the material specific heat at constant pressure, C_p, in its turn, its ability to conduct heat is proportional to the material thermal conductivity, κ. For the Niobium material these properties are related with the temperature by the following equations, for the range of 20 – 2500K:

$$C_p = \frac{23{,}7+4{,}019\times T}{M} \quad [27],$$

$$\kappa = 2 \times 10^{-6} \times T^2 + 0{,}0131 \times T + 45{,}784 \quad [28],$$

where T is the temperature and M the molar mass.

Since the window and conical insert temperature increments reached in the simulations are significant, considering constant niobium thermodynamic properties, could lead to an inaccurate calculation of the temperature raise. Table 7 shows that, for a deployed power of 1000W, the maximum temperatures of the niobium window and conical insert are 285 and 2388 ºC respectively. These temperatures justify the implementation of the niobium specific heat capacity and thermal conductivity dependence with temperature. Thus, a simulation with 1000W of deployed power was made implementing the niobium C_p and k temperature dependence (equations 27 and 28). The simulations consisted on 480 iterations of 0,25s, corresponding to a simulation time of 120s.

Table 6 - Conical insert, liquid target, window and cooling water temperatures for 1000W power deployed for simulations including a constant specific heat capacity and thermal conductivity and temperature dependent.

	Conical Insert			**Liquid target**			**Window**			**Cooling Water**		
	Av. T (ºC)	T_{max} (ºC)	Δ Av. T (ºC)	Av. T (ºC)	T_{max} (ºC)	Δ Av. T (ºC)	Av. T (ºC)	T_{max} (ºC)	Δ T_{max} (ºC)	Av. T (ºC)	Outlet T (ºC)	Δ Outlet T (ºC)
Constant Thermal Properties	77	285	54	1279	2369	1256	798	2388	2365	26.62	27.61	4.61
Temperature Dependent Thermal Properties	79	300	56	1267	2030	1244	764	2043	2020	26.63	27.63	4.63

Table 6 demonstrates that it is crucial to implement the temperature dependence of the thermodynamic properties of niobium. It is clear that although the cooling water temperature is almost unaltered, the maximum temperatures of the remaining domains are strongly influenced. The conical insert maximum temperature increases from 285 to 300ºC, but the most significant result comes when comparing liquid target and window temperature values. Both the window average and maximum temperature decrease about 300ºC when compared with the previous value. This strongly indicates that temperature dependent thermodynamic properties implementation is necessary in order to get accurate results. This way, the maximum temperature observed on the window it is safely distant from the niobium melting point (2477ºC).

The maximum temperature of the liquid target is obtained next to the window (see Figure 27). Therefore, due to the decrease of the window maximum temperature increment, its value varies significantly while its average value remains practically identical. Hence, is clear that the heat generated at the window is transferred to the liquid target.

The proton´s energy deposition profile implementation on the window and liquid target and the outlet cooling water temperature linear increase with current, agree with the expected thermodynamic behaviour of the liquid target system. Therefore, it is possible to affirm that the simulation model can be used to study the liquid target. Thus, the model is suitable to simulate

the influence of the parameters that could lead to the improvement of the target system capacity to remove heat, and consequently increase the radionuclide production.

Chapter III. Results and Discussion

The variables chosen to characterize the liquid target system were the temperatures of the following elements: liquid target, target window, average and outlet cooling water and the conical insert. These metrics enable to study the influence of several parameters of interest on the liquid target system; namely: the temperature of the cooling water inlet, its mass flow rate, the helium temperature and its heat transfer coefficient (equivalent to the mass flow rate). Thermal analysis of the system was conducted by obtaining the average and maximum temperatures, as well as the temperature increments. Table 7 summarizes the results obtained for all these simulations. In order to study the effect of a single variable on the simulation model, the helium and water boundary/initial conditions were kept constant, except the variable of study.

The following simulations were performed with a large deployed power of 1000W, with the purpose to obtain more significant temperature variations and at the same time implement a generated power corresponding to a typical liquid target irradiation. Simulation runs consisted of 480 iterations of 0,25s, corresponding to a simulation time of 120s. Niobium thermodynamic properties were defined as temperature dependent and the initial temperature for all the domains was the same and equal to the cooling water inlet temperature.

Table 7 - Temperatures of the conical insert, liquid target, target window and cooling water for different values of the cooling water mass flow rate (red), cooling water inlet temperature (green), helium heat transfer coefficient (yellow) and helium temperatures (blue).

				Conical Insert			**Liquid target**			**Window**			**Cooling Water**		
Cooling Water Mass Flow Rate (kg/min)	**Cooling Water T (°C)**	**He hc (W/m2 K)**	**He T (°C)**	Av. T (°C)	T_{max} (°C)	Δ Av. T (°C)	Av. T (°C)	T_{max} (°C)	Δ Av. T (°C)	Av. T (°C)	T_{max} (°C)	Δ T_{max} (°C)	Av. T (°C)	Outlet T (°C)	Δ Outlet T (°C)
0.3	23	50	20	155	376	132	1344	2081	1321	831	2094	2071	57,35	67,35	44,35
0.6				125	347	102	1317	2062	1294	806	2075	2052	40,99	46,05	23,05
3				**79**	**300**	**56**	**1267**	**2030**	**1244**	**764**	**2043**	**2020**	**26,63**	**27,63**	**4,63**
15				54	273	31	1243	2012	1220	740	2025	2002	23,72	23,95	0,95
3	15			71	293	56	1259	2025	1244	757	2038	2023	18,65	19,63	4,63
	23			**79**	**300**	**56**	**1267**	**2030**	**1244**	**764**	**2043**	**2020**	**26,63**	**27,63**	**4,63**
	30			86	307	58	1274	2034	1246	769	2047	2019	33,64	34,62	4,62
	23	5	5	80	312	57	1274	2090	1251	794	2103	2080	26,69	27,69	4,69
		50		79	286	56	1277	1897	1254	768	1905	1882	26,72	27,67	4,67
		250		72	257	49	1234	1794	1211	648	1806	1783	26,41	27,33	4,33
		500		68	220	45	1218	1565	1195	545	1576	1553	26,27	27,11	4,11
		5	20	80	312	57	1274	2090	1251	794	2103	2080	26,69	27,69	4,69
		50		**79**	**300**	**56**	**1267**	**2030**	**1244**	**764**	**2043**	**2020**	**26,63**	**27,63**	**4,63**
		250		73	258	50	1236	1797	1213	650	1809	1786	26,42	27,34	4,34
		500		67	222	44	1210	1570	1187	549	1581	1558	26,24	27,12	4,12

Cooling Water Mass Flow Rate

Figure 34 illustrates the influence of the flow rate of the cooling water on the parameters of interest. It is noticeable that increasing the water-cooling mass flow rate from the 3 to 15kg/min, decreases the temperatures of all the domains. Specifically, the mass flow rate presents a critical influence on the average temperatures of the outlet cooling water and on the conical insert. The first observation can be explained by the fact that, due to the mass conservation, for a larger mass flow rate, the water´s velocity through the water channels increases, resulting in a reduced time of the contact between the cooling water and the conical insert. Therefore, the cooling water temperature increases less when compared with the standard mass flow rate (3kg/min). On the other hand, the conical insert temperature decrease it is explained by the greater heat transfer from the conical insert to the cooling water, due to the increase of the Nusselt number associated with the water larger velocity. In other words, the convective heat transfer is proportional to Nu, which in turn, is proportional to the fluid velocity. On the other hand, the maximum window and average liquid target temperature reduction is 18 and 24ºC, respectively. Comparing these values with the temperatures of thousands of Celsius of these domains, it is possible to conclude that the cooling water mass flow rate is capable of influencing the window and liquid target temperatures, although, this effect is not that significant.

Considering now the lowest water-cooling mass flow rate values, i.e. 0,3 and 0,6 kg/min, it is worth noticing that the average conical insert, outlet and liquid target temperature increments are significantly larger, when compared to the values for the standard 3kg/min. Also, the maximum window temperature increment is lower than for the other domains. The fact that the window is the less influenced by the cooling water mass flow rate can be explained by the fact that the cooling water flow is distant from the window location. It is then possible to conclude that it is necessary to guarantee that the water mass flow rate responsible for removing the heat of the liquid target system, is at least 3kg/min.

Overall, increasing the mass flow rate of the cooling water proves to reduce the temperatures of the liquid target system. Thus, it is possible to affirm, that it may be used to improve the capacity to remove heat form the system.

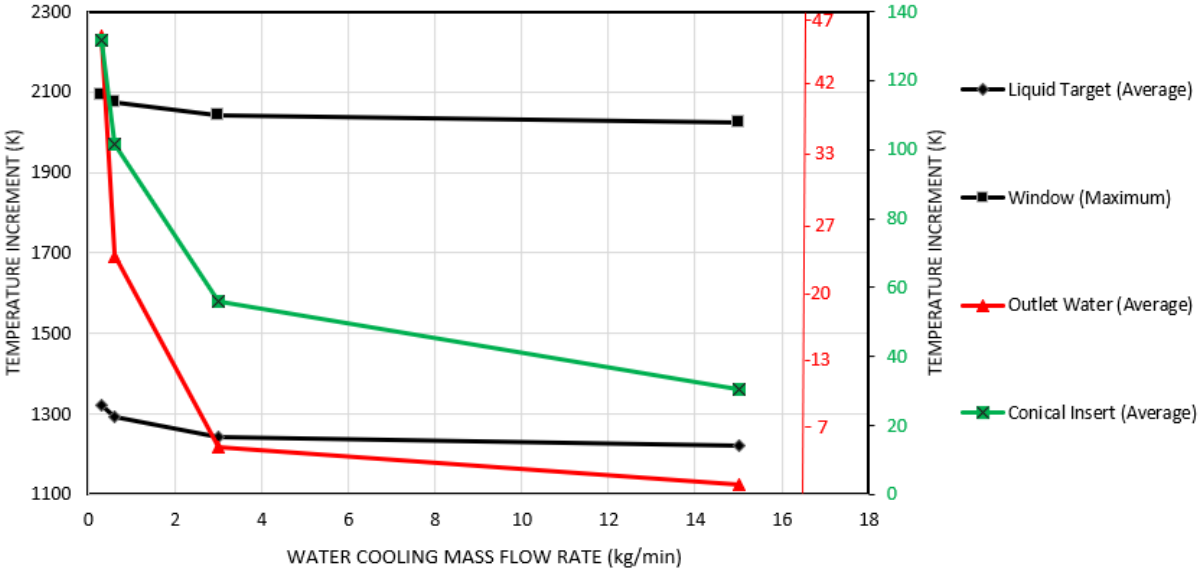

Figure 34 - Average temperature increments for the liquid target, outlet water and conical insert and maximum temperature increment of the window, for different values of the water-cooling mass flow rate. All increments are related to the initial temperature of 296,15K.

Cooling Water Inlet Temperature

It was verified that the effect of the cooling water inlet temperature on the window, conical insert and liquid target temperature was basically null (see figure 35 and table 7). On Table 7, it is possible to observe that for distinct inlet temperatures, the outlet average temperature increases accordingly with the inlet temperature, but the temperature increment is practically the same for the three cases. Figure 32 shows that the temperature increments for all these domains is constant and no significant temperature variations were observed. Figure 32 is in agreement with the result experimentally obtained by (46), where, , the temperature increment on the cooling water is almost independent of its initial absolute temperature. This result can be explained by the fact that, the heat transfer from the liquid target to the conical insert and consecutively to the cooling water is proportional to the contact area, the heat transfer coefficient and the temperature difference, as dictated by equation 11. Hence, given constant

area of contact and h_c, the heat transfer only depends on the temperature difference. Table 7 demonstrates that the temperature differential between the conical insert and the cooling water, for the different water inlet temperatures, remains practically constant. This result supports the idea that, the capacity to remove heat of the target system only depends on the area of contact between the cooling water and the niobium conical insert.

Hence, it is possible to affirm that the cooling water inlet temperature present a small influence on the thermal performance of the liquid target system and consequently, it cannot be considered in order to improve the capacity to remove heat.

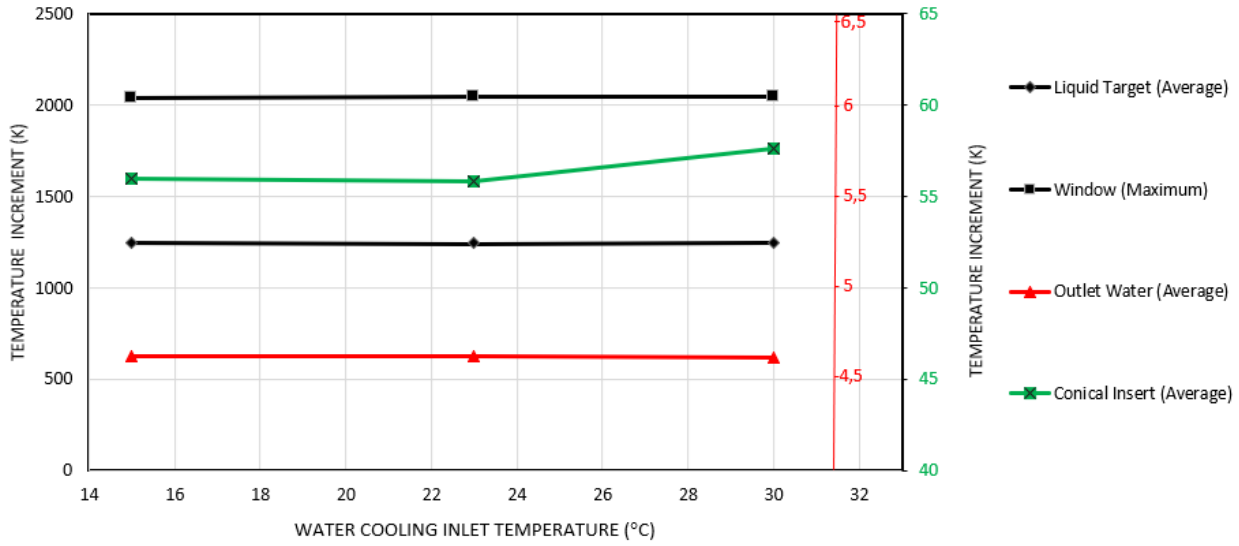

Figure 35 - Average temperature increments for the liquid target, outlet water and conical insert and maximum temperature increment of the window, for different values of the water cooling inlet temperature. All increments are related to the cooling water inlet temperature.

Cooling Helium Temperature and Heat Transfer Coefficient

Although mandatory thin to enable the proton beam to reach the liquid target, the target window has to be simultaneously resistant at the same time in order to sustain the pressure developed inside the liquid target. As previously mentioned, the proton current generates a great amount of heat on the window, which in turn, is continuously removed by the flow of helium. Simulation runs were performed with the aim of studying how the temperature of the liquid

target system domains, especially for the window, is influenced by both the helium initial temperature and the heat transfer coefficient associated with the convective heat transfer.

Figure 36 demonstrates that for a certain value of hc, the temperature increments for the niobium and water domains, are very similar, for different helium temperature values, i.e., for 5 and 20ºC. This result indicates that there is no significant advantage to decrease the helium temperature with the purpose to remove heat. The only exception occurs for a hc of 50 W/m2K, where the window average temperatures increments are 1882ºC with a helium temperature of 5ºC, and 2020ºC with 20ºC. For the remaining heat transfer coefficient values, the similar value of the liquid target average temperature increment can be explained by the fact that, for the value of a h_c of 5 W/m2 K, the heat transferred to the cooling helium is small overlapping the helium temperature effect. On the other hand, for the values of 250 and 500 W/m2K, the explanation for the non-present temperature difference, is exactly the opposite, the cooling helium capacity to remove heat is large enough to overlap the helium temperature effect. In summary, decreasing the helium temperature proves to be only viable for the heat transfer coefficient value of 50 W/m2K, which is exactly the value calculated based on the liquid target system helium flow properties.

Figure 36 enable to observe that the helium heat transfer coefficient presents a strong influence on the temperatures increments. Both for water and niobium domains, the temperature increments decrease with h_c. Although the temperature reductions are smaller in the conical insert and the outlet cooling water, these are significantly larger for the liquid target and mainly for the window. Regarding the liquid target, comparing the temperature increment for the h_c value of 50 with 250 W/m^{2}K, for a helium temperature of 20ºC, there is a reduction of 57ºC. This result proves that more heat is being removed from the liquid target and, the pressure developed inside the conical insert will be consequently smaller. Therefore, it is possible to increase the target current, i.e., the radionuclide production. Nonetheless, the most important result prevails on the reduction of the temperature increment of the target window, where for a helium temperature of 20ºC, the temperature increment decreases from 2043 to 1581ºC, for a h_c value of 50 and 250 W/m^{2}K respectively. This result is extremely positive, considering that the window is the most sensitive part of the target system. Due to the beam focusing on the centre of the window (beam diameter of 9,5mm) and the fact that it is so thin, there is a propensity to rupture under high pressure, resulting in the target failure.

In summary, improving the heat transfer coefficient effectively decreases the window maximum temperature.

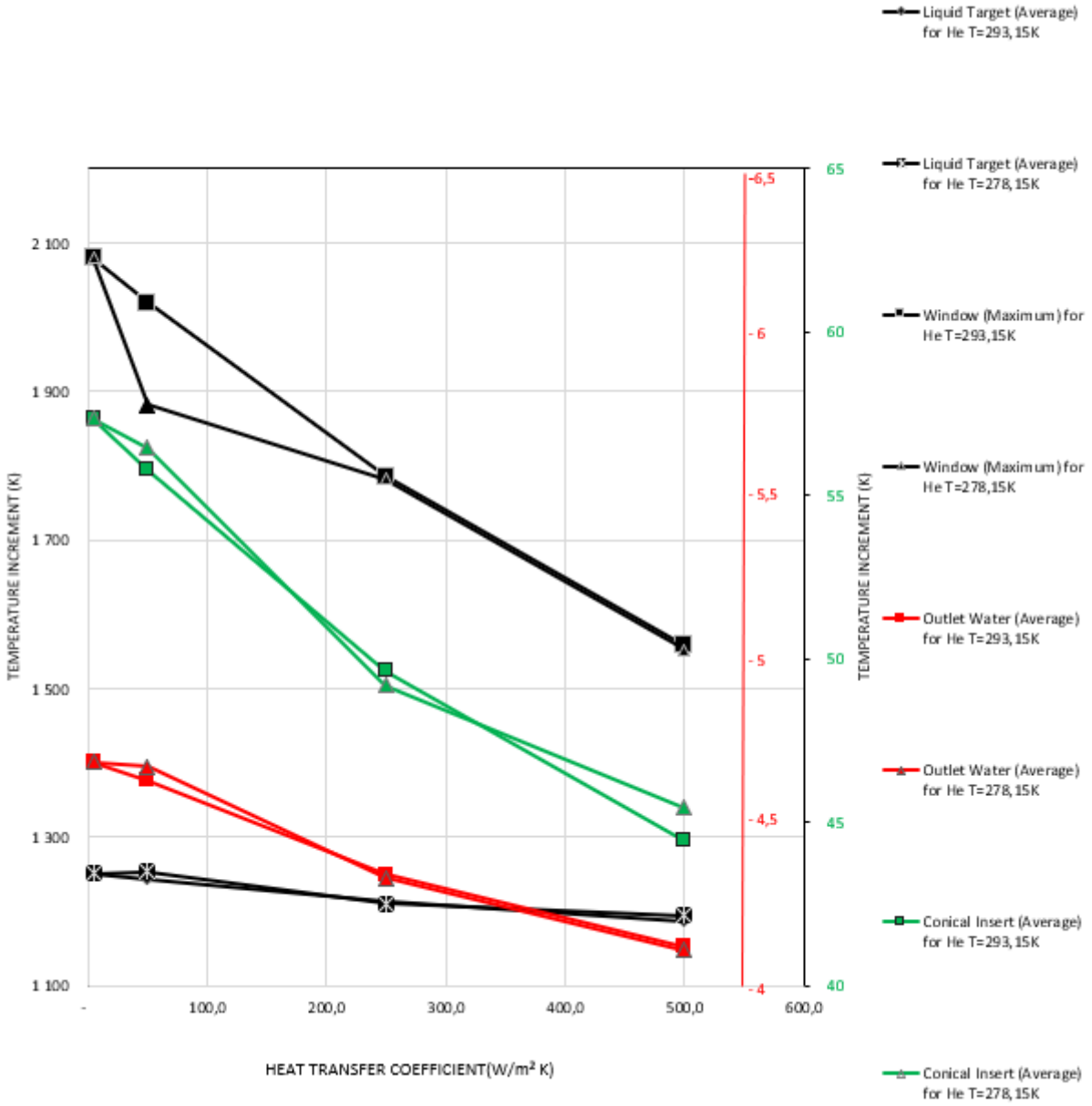

Figure 36 - Average temperature increments for the liquid target, outlet water and conical insert and maximum temperature increment of the window, for different values of the helium heat transfer coefficient and helium temperature, namely 278,25 and 293,15K. All increments are related to the initial temperature of 296,15K.

For the helium cooling system of the present liquid target, the heat transfer coefficient is proportional to the helium mass flow rate. In other words, increasing the helium density or velocity, would lead to the increase of h_c, and consecutively, improve the convective heat transfer. Based on the obtained results it is possible to admit that the capacity to remove heat would be significantly improved by increasing the mass flow rate of helium between the target

windows. However, it is important to notice that larger helium densities lead to more significant interference with the beam. Therefore, it is mandatory to ensure that the helium mass flow rate is the larger value possible and at the same time does not stop the beam.

Chapter IV. Conclusion and Future Work

Conclusion

In this thesis, a CFD simulation model relying on FEM was developed in order to replicate the thermal behaviour of a cyclotron liquid target system. The thick niobium target window used in the production of radiometals was implemented and studied. The energy deposition profile of the proton beam was calculated through Monte Carlo simulation method on SRIM software and was posteriorly implemented trough energy sources and functions delimiting its geometry. Furthermore, the cooling systems responsible for removing the heat generated by the beam were also implemented and characterized by boundary conditions.

The main focus of the present thesis was to validate the model developed and to study the influence of the main parameters of the system on the thermal performance of the target, with the primary objective to improve the removing heat capacity to enable an increase of the radionuclide production. Validation of the developed platform was made by comparing the cooling water outlet temperatures for different target current values with the ones obtained experimentally in (46). It was possible to conclude that cooling water outlet temperature increased linearly with the target current, at a rate increment quantitively similar to the ones obtained by do Carmo. S, i.e., around ±1ºC per 10 μA.

The mass flow rate and initial temperature of the cooling water, together with the helium temperature and heat transfer coefficient were the selected variables of the present study. In order to evaluate their effect on the liquid target system, average and maximum temperatures were obtained and analyzed. The major conclusions concerning the cooling water effect are that its initial temperature does not influence the target system thermal behaviour. On the other hand, the present water mass flow rate implemented on the liquid target system should be increased, since it was observed that it is capable of improving the heat removed from the system. It was also verified that for mass flow rates lower than 3kg/min, the temperature of the

liquid target domains increased significantly. Considering that this value corresponds to the mass flow rate implemented in the cyclotron liquid target system, one can conclude that the mass flow rate of the cooling water should be at least 3kg/min.

Helium responsible to cool the target window revealed to be relevant on the liquid target thermal performance. Although the helium temperature presents no significant effect on the window temperature, higher values of hc, significantly reduce the window and liquid target temperatures. Considering that window rupture is the main cause of target failure and also that the liquid target temperature reduction will reflect on a lower pressure inside the target, this result indicates that there is interest in improving the cooling helium system, namely by increasing the helium mass flow rate.

In conclusion, the simulation platform was proved to characterize the target system as intended. Relevant results were obtained concerning the liquid target system thermal performance. These results could contribute to the development of methods that would improve the capacity to remove heat. This will allow to increase the target current and consequently, increase the production yield.

Future Work

Considering this to be a first approach of a model of the liquid target thermodynamic performance, many features could be explored in future work. To fully model the thermal performance of the liquid target it is necessary to consider the phase change processes occurring inside the conical insert and implement the presence of air and steam. The thermal performance of the liquid target would be influenced by the existence of multiple phases, and mainly by the water-steam phase change process. Since both air and steam exist on the gaseous state, the thermal conductivity would be significantly smaller. In order to improve the accuracy of the simulation, water thermodynamic properties should be temperature dependent, this could be modelled by the IAWPS material implementation (48). The modelling of a multiphase simulation will introduce the need to model the interphase momentum transfer for the existent phases, namely the drag, lift, virtual mass, wall lubrification and turbulent

dispersion force resulting from the continuous/dispersed phases interaction (51). Water-steam phase change could be modelled by the previously existing models on ANSYS or by user defined mass, sink and energy sources which define the mass transfer between water and steam, while also considering the latent heat resulting from phase change. Another important consideration would be the interphase heat transfer modelling, since the Nusselt number and consequently, the heat transferred for each phase will depend on the phase change process occurring inside the target. Also, the pressure developed inside the conical insert would enable further validation of the simulation model, since it would be possible to compare the results with the experimentally measured pressures as function of the proton current.

Another study of great interest would be to test different turbulence models, both on the liquid target and cooling water. Since each model is suitable for different phenomena, it would be required to deeply study how the near wall treatment influences the fluid velocity and the heat transfer at the boundaries, for both fluid domains.

The improvement of the capacity to remove heat of the cooling water is also directly related with the area of contact between the conical insert and the cooling water and with the conical insert thermal thickness and thermal conductivity. Therefore, it would be interesting to investigate materials with different thermodynamic properties for the conical insert and also study various designs for the target insert, as well for the cooling water channels.

At last, the coupling with an external software responsible for calculating the beam energy deposition profile, in order to update the implementation of the generated power and the resulting local density variation for every iteration, would increase the accuracy of the simulation.

References

1. ALVES, F., ALVES, V. H. P., DO CARMO, S. J. C., NEVES, A. C. B., SILVA, M. and ABRUNHOSA, A. J. Production of copper-64 and gallium-68 with a medical cyclotron using liquid targets. *Modern Physics Letters A*. 2017. DOI 10.1142/S0217732317400132. This work describes the production of two clinically relevant metal radioisotopes 64Cu and 68Ga with a medical cyclotron by the irradiation of liquid targets. New results are presented for the implementation of this methodology in a fully automated system, using commercially available equipment. Liquid target solutions containing enriched 64Ni and 68Zn were loaded, bombarded and transferred to synthesis modules where a purified solution containing the desired radiometal is obtained and can then be used to further radiolabeling within only one hour after End-Of-Bombardment (EOB). Typical production runs using enriched material lead to the production of 5 GBq and 6 GBq (0.14 MBq/(μAh · mg) and 1.5 MBq/(μAh · mg)) of 64Cu and 68Ga; although the technique can be used to obtain up to 25 GBq and 40 GBq, respectively, by simply scaling up the amount of the enriched material. Purified solutions containing 64Cu and 68Ga were obtained within 30 min after EOB and used to produce 64Cu-ATSM and 68Ga–DOTA–NOC, respecti...
2. ALVES, Vítor, DO CARMO, Sérgio, ALVES, Francisco and ABRUNHOSA, Antero. Automated Purification of Radiometals Produced by Liquid Targets. *Instruments*. 2018. DOI 10.3390/instruments2030017. An automated process for the production and purification of radiometals produced by irradiating liquid targets in a medical cyclotron, using a commercially available module, has been developed. The method is suitable for the production and purification of radiometals such as 68Ga, 64Cu and 61Cu through irradiation of liquid targets and is important for producing high specific activity radioisotopes with a substantial reduction in processing time and cost when compared with the solid target approach. The “liquid target” process also eliminates the need for pre- and post-irradiation target preparation and simplifies the transfer of irradiated material from target to hotcell. A 68GaCl3 solution can be obtained in about 35 min with an average yield of 73.9 ± 6.7% in less than 10 mL of volume. 64CuCl2 solutions can be obtained with an average yield of 81.2 ± 7.8% in about 1 h of processing time. A dedicated single-use disposable kit is used on a commercial IBA Synthera® extension module.
3. I., E., STRANG, Gilbert and FIX, George J. An Analysis of the Finite Element Method. *Mathematics of Computation*. 2006. DOI 10.2307/2005716. An introduction to the theory -- A summary of the theory -- Approximation -- Variational crimes -- Stability -- Eigenvalue problems -- Initial-value problems -- Singularities.
4. OBERKAMPF, William L, TRUCANO, Timothy G and HIRSCH, Charles. Verification, validation, and predictive capability in computational engineering and physics. *Applied Mechanics Reviews*. 2004. DOI 10.1115/1.1767847. The views of state of art in verification and validation (V & V) in computational physics are discussed. These views are described in the framework in which predictive capability relies on V & V, as well as other factors that affect predictive capability. Some of the

research topics addressed are development of improved procedures for the use of the phenomena identification and ranking table (PIRT) for prioritizing V & V activities, and the method of manufactured solutions for code verification. It also addressed development and use of hierarchical validation diagrams, and the construction and use of validation metrics incorporating statistical measures.

5. CHAI, J.S., HA, J.H., LEE, H.Y., KIM, Y.S., OH, S. and YOON, M. New design and development of 13 MeV PET cyclotron in Korea. In : . 2003. Since 1997 design studies have been in progress in a joint collaboration between the Korea Cancer Center Hospital (KCCH) and the Pohang University of Science and Technology (POSTECH) for a 13 MeV PET (Positron Emission Tomography) cyclotron. It will accelerate H- (negatively charged hydrogen) ions, which, after acceleration, will be stripped of its electrons by a stripping foil and then, on entering the target chamber, interact with the target material to produce positron emitters such as 18F, 15O, 13N and 11C. In this paper we describe the main features of the cyclotron.
6. SILVA, Magda Filipa Carvalho. Application of ICP-MS in the optimisation of a new methodology for 68 Ga production in a PET dedicated cyclotron. . 2016.
7. CHOU, W., LACKEY, J., TANG, Z., YOON, P. and KOSTIN, M. Some physics issues of carbon stripping foils. In : *Proceedings of the IEEE Particle Accelerator Conference*. 2007. ISBN 1424409179.
8. DEVILLET, F., GHYOOT, J., M., M. Geets, KRAL, E., NACTERGAL, B., MOOIJ, R. and M.VOSJAN. PERFORMANCE OF IBA NEW CONICAL SHAPED NIOBIUM [18O] WATER TARGETS. *In Proceedings of the 15th international Worshop on Targetryand Target Chemistry—WTTC, Prague, Czech Republic, 18–21*. 2014.
9. DEVILLET, F, GEETS, J, GHYOOT, M, KRAL, E, NACTERGAL, B, MOOIJ, R and VOSJAN, M. Performance of Iba New Conical Shaped Niobium [18 O] Water Targets. *In Proceedings of the 15th international Worshop on Targetry and Target Chemistry—WTTC, Prague, Czech Republic*. 2014. P. 145–148.
10. Table of Thermal neutron Cross Sections of the Isotopes. [online]. 1960. [Accessed 20 June 2019]. Available from: https://link.springer.com/content/pdf/bbm%3A978-3-642-87614-1%2F1.pdf
11. HESS, E, TAKÁCS, Sándor, SCHOLTEN, Bernhard, TARKANYI, F, H. COENEN, Heinz and QAIM, Syed. Excitation function of the 18O(p,n)18F nuclear reaction from threshold up to 30 MeV. *Radiochimica Acta - RADIOCHIM ACTA*. 2001. Vol. 89. DOI 10.1524/ract.2001.89.6.357.
12. ALVES, F., ALVES, V. H. P., DO CARMO, S. J. C., NEVES, A. C. B., SILVA, M. and ABRUNHOSA, A. J. Production of copper-64 and gallium-68 with a medical cyclotron using liquid targets. *Modern Physics Letters A*. 2017. DOI 10.1142/S0217732317400132. This work describes the production of two clinically relevant metal radioisotopes 64Cu and 68Ga with a medical cyclotron by the irradiation of liquid targets. New results are presented for the implementation of this methodology in a fully automated system, using commercially available equipment. Liquid target solutions containing enriched 64Ni and 68Zn were loaded, bombarded and transferred to synthesis modules where a purified solution containing the desired radiometal is obtained and can then be used to further radiolabeling within only one hour after End-Of-Bombardment (EOB). Typical production runs using enriched material lead to the production of 5 GBq and 6 GBq (0.14 MBq/(μAh · mg) and 1.5 MBq/(μAh · mg)) of 64Cu and 68Ga; although the technique can be used to obtain up to 25 GBq and 40 GBq, respectively, by simply scaling up the amount of the enriched

material. Purified solutions containing 64Cu and 68Ga were obtained within 30 min after EOB and used to produce 64Cu-ATSM and 68Ga–DOTA–NOC, respecti...

13. ALLONI, D., PRATA, M. and SMILGYS, B. Experimental and Monte Carlo characterization of radionuclidic impurities originated from proton irradiation of [18 O]H 2 O in a modern medical cyclotron. *Applied Radiation and Isotopes*. 2019. DOI 10.1016/j.apradiso.2019.01.026. In this work we present a characterization of the radionuclidic impurities originated by proton irradiation of enriched water [18 O]H 2 O in a medical cyclotron through Monte Carlo simulations and experimental measurements. A set of standard samples of enriched water loaded in the cyclotron target cell have been irradiated at 30 μA proton current for 1 h each and, after an appropriate cooling time, measured by HPGe gamma spectrometry. In this way it was possible to study the direct release of radionuclidic impurities from target components as well as the release as a function of target ageing. Previously to experimental measurements, Monte Carlo calculations with the PHITS Code have been carried out to estimate the radionuclides generated within the target components (in particular Havar ® foil) with the aim to identify the nuclides expected to be found in the irradiated water due to cell-to-water transmission mechanisms. Comparison between simulations data and experimental measurements by gamma spectrometry showed that only a very small amount of the radionuclides produced in the target window are released in the enriched water through corrosion/erosion effects, while the release decreases with increasing aging of the target.
14. LEO, WR. *Techniques for Nuclear and Particle Physics Experiments*. 1987. ISBN 978-3-540-57280-0. 2nd rev. ed. 1. Basic Nuclear Processes in Radioactive Sources -- 2. Passage of Radiation Through Matter -- 3. Radiation Protection. Biological Effects of Radiation -- 4. Statistics and the Treatment of Experimental Data -- 5. General Characteristics of Detectors -- 6. Ionization Detectors -- 7. Scintillation Detectors -- 8. Photomultipliers -- 9. Scintillation Detector Mounting and Operation -- 10. Semiconductor Detectors -- 11. Pulse Signals in Nuclear Electronics -- 12. The NIM Standard -- 13. Signal Transmission -- 14. Electronics for Pulse Signal Processing -- 15. Pulse Height Selection and Coincidence Technique -- 16. Electronic Logic for Experiments -- 17. Timing Methods and Systems -- 18. Computer Controlled Electronics: CAMAC -- App. A.A Review of Oscilloscope Functions -- App. B. Physical and Numerical Constants -- App. C. Resistor Color Code.
15. EL GHAZALY, M. and HASSAN, H. E. Spectroscopic studies on alpha particle-irradiated PADC (CR-39 detector). *Results in Physics*. 2014. DOI 10.1016/j.rinp.2014.04.001. Spectroscopic studies on a Poly Allyl Diglycol Carbonate (PADC or CR-39) detector irradiated with 5MeV α-particles were carried out. The CR-39 samples were exposed to perpendicular incidence of α-particles with different fluence ranging from 0.85×109 to 6.79×109particles/cm2. The induced modifications in the CR-39 detectors were investigated using UV-Vis, FTIR, and photoluminescence (PL) spectroscopy. The results reveal that UV-Visible and FTIR spectroscopic techniques are insensitive to detect the induced modifications in the irradiated CR-39 detector within the selected range of fluence. Photoluminescence (PL) spectra, on the other hand, showed a reasonable difference between the detected spectra of the irradiated samples. The integrated intensity (N) under the PL emission band and peak's heights (P) exhibits a linear correlation with the alpha particles fluence. The fitting linear formula and the relevant parameters for both relations (N and P vs. fluence) were determined. The comparison study between the three spectroscopic techniques indicated that PL spectroscopy provides a sensitive method for α-particles

dosimetric applications using a CR-39 detector. © 2014 The Authors.
16. ZIEGLER, James F., ZIEGLER, M. D. and BIERSACK, J. P. SRIM - The stopping and range of ions in matter (2010). *Nuclear Instruments and Methods in Physics Research, Section B: Beam Interactions with Materials and Atoms*. 2010. DOI 10.1016/j.nimb.2010.02.091. SRIM is a software package concerning the Stopping and Range of Ions in Matter. Since its introduction in 1985, major upgrades are made about every six years. Currently, more than 700 scientific citations are made to SRIM every year. For SRIM-2010, the following major improvements have been made: (1) About 2800 new experimental stopping powers were added to the database, increasing it to over 28,000 stopping values. (2) Improved corrections were made for the stopping of ions in compounds. (3) New heavy ion stopping calculations have led to significant improvements on SRIM stopping accuracy. (4) A self-contained SRIM module has been included to allow SRIM stopping and range values to be controlled and read by other software applications. (5) Individual interatomic potentials have been included for all ion/atom collisions, and these potentials are now included in the SRIM package. A full catalog of stopping power plots can be downloaded at www.SRIM.org. Over 500 plots show the accuracy of the stopping and ranges produced by SRIM along with 27,000 experimental data points. References to the citations which reported the experimental data are included.
17. The binary collision approximation: Background and introduction. *Radiation Effects and Defects in Solids*. 1994. DOI 10.1080/10420159408219767. The binary collision approximation (BCA) has long been used in computernsimulations of the interactions of energetic atoms with solid targets,nas well as being the basis of most analytical theory in this area.nWhile mainly a high-energy approximation, the BCA retains qualitativensignificance at low energies and, with proper formulation, givesnuseful quantitative information as well. Moreover, computer simulationsnbased on the BCA can achieve good statistics in many situations wherenthose based on full classical dynamical models require the most advancedncomputer hardware or are even impracticable.nnnThe foundations of the BCA in classical scattering are reviewed, includingnmethods of evaluating the scattering integrals, interaction potentials,nand electron excitation effects. The explicit evaluation of timenat significant points on particle trajectories is discussed, as arenscheduling algorithms for ordering the collisions in a developingncascade. An approximate treatment of nearly simultaneous collisionsnis outlined and the searching algorithms used in MARLOWE are presented.
18. HOFSÄSS, H., ZHANG, K. and MUTZKE, A. Simulation of ion beam sputtering with SDTrimSP, TRIDYN and SRIM. *Applied Surface Science*. 2014. DOI 10.1016/j.apsusc.2014.03.152. A quantitative simulation of ion beam sputtering and related collision cascade effects is essential for applications of ion beam irradiation in thin film deposition, surface treatment and sculpting with focused ion beams, ion beam smoothing of surfaces and ion-induced nanopattern formation. The understanding of fundamental ion-solid interaction processes relevant for nanostructure formation, ion-induced mass redistribution, sputter yield amplification, ion beam mixing and dynamic compositional changes requires reliable simulations of ion-solid interaction processes in particular at low ion energies. In this contribution we discuss the possibilities, the key benefits and the limitations of three popular binary collision Monte Carlo simulation programs (SDTrimSP, TRIDYN and SRIM). The focus will be set to the calculation of angle dependent sputter yields, angular distribution of sputtered particles, sputter yields for compound materials, sputter yield amplification effects, as well as the extraction of parameters relevant for modeling ion-induced surface pattern

formation from vacancy and recoil atom distributions. © 2014 Elsevier B.V.

19. INCROPERA, Frank P, DEWITT, David P, BERGMAN, Theodore L and LAVINE, Adrienne S. *Fundamentals of Heat and Mass Transfer 6th Edition*. 2007. ISBN 9780471457282. This bestselling book in the field provides a complete introduction to the physical origins of heat and mass transfer. Noted for its crystal clear presentation and easy-to-follow problem solving methodology, Incropera and Dewitt's systematic approach to the first law develops reader confidence in using this essential tool for thermal analysis. Readers will learn the meaning of the terminology and physical principles of heat transfer as well as how to use requisite inputs for computing heat transfer rates and/or material temperatures.
20. DATT, Prem. Latent heat of vaporization/condensation. In : *Encyclopedia of Earth Sciences Series*. 2011. Predicting the binding mode of flexible polypeptides to proteins is an important task that falls outside the domain of applicability of most small molecule and protein−protein docking tools. Here, we test the small molecule flexible ligand docking program Glide on a set of 19 non-α-helical peptides and systematically improve pose prediction accuracy by enhancing Glide sampling for flexible polypeptides. In addition, scoring of the poses was improved by post-processing with physics-based implicit solvent MM- GBSA calculations. Using the best RMSD among the top 10 scoring poses as a metric, the success rate (RMSD ≤ 2.0 Å for the interface backbone atoms) increased from 21% with default Glide SP settings to 58% with the enhanced peptide sampling and scoring protocol in the case of redocking to the native protein structure. This approaches the accuracy of the recently developed Rosetta FlexPepDock method (63% success for these 19 peptides) while being over 100 times faster. Cross-docking was performed for a subset of cases where an unbound receptor structure was available, and in that case, 40% of peptides were docked successfully. We analyze the results and find that the optimized polypeptide protocol is most accurate for extended peptides of limited size and number of formal charges, defining a domain of applicability for this approach.
21. MESEGUER, José, PÉREZ-GRANDE, Isabel and SANZ-ANDRÉS, Angel. Thermal radiation heat transfer. In : *Spacecraft Thermal Control*. 2012. Providing a comprehensive overview of the radiative behavior and properties of materials, the fifth edition of this classic textbook describes the physics of radiative heat transfer, development of relevant analysis methods, and associated mathematical and numerical techniques. Retaining the salient features and fundamental coverage that have made it popular, Thermal Radiation Heat Transfer, Fifth Edition has been carefully streamlined to omit superfluous material, yet enhanced to update information with extensive references. Includes four new chapters on Inverse Methods, Electromagnetic Theory, Scattering and Absorption by Particles, and Near-Field Radiative TransferKeeping pace with significant developments, this book begins by addressing the radiative properties of blackbody and opaque materials, and how they are predicted using electromagnetic theory and obtained through measurements. It discusses radiative exchange in enclosures without any radiating medium between the surfaces—and where heat conduction is included within the boundaries. The book also covers the radiative properties of gases and addresses energy exchange when gases and other materials interact with radiative energy, as occurs in furnaces.To make this challenging subject matter easily understandable for students, the authors have revised and reorganized this textbook to produce a streamlined, practical learning tool that:Applies the common nomenclature adopted by the major heat transfer journalsConsolidates past material, reincorporating much of the previous text into appendicesProvides an

updated, expanded, and alphabetized collection of references, assembling them in one appendixOffers a helpful list of symbolsWith worked-out examples, chapter-end homework problems, and other useful learning features, such as concluding remarks and historical notes, this new edition continues its tradition of serving both as a comprehensive textbook for those studying and applying radiative transfer, and as a repository of vital literary references for the serious researcher.

22. SABHARWALL, Piyush, UTGIKAR, Vivek and GUNNERSON, Fred. Effect of Mass Flow Rate on the Convective Heat Transfer Coefficient: Analysis for Constant Velocity and Constant Area Case. *Nuclear Technology*. 2017. DOI 10.13182/nt09-a7406. The effect of the mass flow rate at constant velocity on the convective heat transfer coefficient of an incompressible fluid in a turbulent flow regime is presented with the help of dimen- sional analysis. The heat transfer coefficient decreases by ~10% with a threefold increase in the mass flow rate under these conditions, based on the commonly used Dittus-Boelter corre- lation for estimation of the heat transfer coefficient. On the other hand, an increase in the heat transfer coefficient is ob- served if the area is maintained constant. Doubling the mass flow rate will result in a 92% increase in the heat transfer coefficient. However, there is a concomitant increase in the pressure drop, proportional to the mass flow rate raised to 0.95. The pressure drop is predicted to decrease for the con- stant velocity case with an inverse dependence on the mass flow rate. The pressure drop considerations may be critical in certain situations (elevation of boiling point in case of a boil- ing heat transfer medium), and any benefit derived from the higher heat transfer coefficient may be lost because of the higher pressure drop across the heat exchanger in the constant area case.
23. GOSMAN, A. D. Developments in CFD for industrial and environmental applications in wind engineering. *Journal of Wind Engineering and Industrial Aerodynamics*. 1999. DOI 10.1016/S0167-6105(99)00007-0. An overview is provided of the capabilities and limitations of CFD as a tool for wind engineering, with particular reference to commercial CFD codes. The status of the modelling of turbulence, heat and mass transfer is briefly reviewed and developments in computer solution methodology are outlined, with emphasis on geometry-handling and mesh-generation capabilities and parallel computing. Examples are shown of recent applications in the built environment and other industries which illustrate the current state of art. The overall conclusion is that, although there are well-known weaknesses in the physics modelling, the level of prediction accuracy is already sufficient for some purposes. © 1999 Elsevier Science Ltd. All rights reserved.
24. DING, H., VISSER, F. C., JIANG, Y. and FURMANCZYK, M. Demonstration and Validation of a 3D CFD Simulation Tool Predicting Pump Performance and Cavitation for Industrial Applications. In : *Volume 1: Symposia, Parts A, B and C*. 2009. ISBN 978-0-7918-4372-7. Due to complexities in geometry and physics, computational fluid dynamics (CFD) pump simulation has historically been very challenging and time consuming, especially for cases with cavitation. However, with the evolution and innovation of CFD technologies, pump cavitation simulation has improved significantly in recent years. In view of these developments, this paper will discuss a new generation CFD tool for pump cavitation simulation, using an axial flow water pump as a demonstration case. A novel CFD methodology and advanced cavitation model will be presented and discussed. Key com-ponents that are relevant to the improvement of accuracy and CFD simulation speed will be discussed in detail. An axial flow water pump is chosen as the test case to demonstrate and validate the capability and accuracy of the code discussed. Simulation results include pump head,

hydraulic efficiency, and cavitation characteristic in terms of incipient net positive suction head for the whole pump flow passages using both multiple reference frame and transient approaches. Multiple operation conditions, from 70% to 120% of duty flow rate, have been evaluated and will be projected against experimental data. Furthermore, simulated cavitation patterns will be compared with video images recorded during the experiments.

25. MILEWSKA, A. and MOLGA, E. J. CFD simulation of accidents in industrial batch stirred tank reactors. *Chemical Engineering Science*. 2007. DOI 10.1016/j.ces.2006.12.036. In this work, we have analyzed the application of CFD (computational fluid dynamics) to simulate consequences of stirrer failures, which can lead to reactor thermal runaway. For a typical industrial batch reactor, several “CFD computational experiments” have been carried out to explore runaway and non-runaway situations. Then the results of the CFD simulations, supported by an on-line divergence criterion, have been used to detect a dangerous reactor behavior. It has been found out, that even for the reactor operated at potentially safe conditions a failure of the stirring system can lead to serious thermal runaways. A significance of a proper location of temperature probe for an early runaway detection has also been discussed. A modification of the applied divergence criterion to avoid false alarms has been proposed and tested. © 2007 Elsevier Ltd. All rights reserved.
26. WENDT, John F., ANDERSON, John D., DEGROOTE, Joris, DEGREZ, Gérard, DICK, Erik, GRUNDMANN, Roger and VIERENDEELS, Jan. *Computational fluid dynamics: An introduction*. 2009. ISBN 9783540850557. The book provides an elementary tutorial presentation on computational fluid dynamics (CFD), emphasizing the fundamentals and surveying a variety of solution techniques whose applications range from low speed incompressible flow to hypersonic flow. It is aimed at persons who have little or no experience in this field, both recent graduates as well as professional engineers, and will provide an insight to the philosophy and power of CFD, an understanding of the mathematical nature of the fluid dynamics equations, and a familiarity with various solution techniques. For the third edition the text has been revised and updated.
27. ZIENKIEWICZ, Olek, TAYLOR, Robert and ZHU, J. Z. *The Finite Element Method: its Basis and Fundamentals: Seventh Edition*. 2013. ISBN 9781856176330. The Finite Element Method: Its Basis and Fundamentals offers a complete introduction to the basis of the finite element method, covering fundamental theory and worked examples in the detail required for readers to apply the knowledge to their own engineering problems and understand more advanced applications. This edition sees a significant rearrangement of the bookâ??s content to enable clearer development of the finite element method, with major new chapters and sections added to cover: Weak forms Variational forms Multi-dimensional field problems Automatic mesh generation Plate bending and shells Developments in meshless techniques Focusing on the core knowledge, mathematical and analytical tools needed for successful application, The Finite Element Method: Its Basis and Fundamentals is the authoritative resource of choice for graduate level students, researchers and professional engineers involved in finite element-based engineering analysis. © 2013 Elsevier Ltd All rights reserved.
28. MADENCI, Erdogan and GUVEN, Ibrahim. *The finite element method and applications in engineering using ANSYS®, second edition*. 2015. ISBN 9781489975508. © Springer International Publishing 2015. This textbook offers theoretical and practical knowledge of the finite element method. The book equips readers with the skills required to analyze engineering problems using ANSYS®, a

commercially available FEA program. Revised and updated, this new edition presents the most current ANSYS® commands and ANSYS® screen shots, as well as modeling steps for each example problem. This self-contained, introductory text minimizes the need for additional reference material by covering both the fundamental topics in finite element methods and advanced topics concerning modeling and analysis. It focuses on the use of ANSYS® through both the Graphics User Interface (GUI) and the ANSYS® Parametric Design Language (APDL). Extensive examples from a range of engineering disciplines are presented in a straightforward, step-by-step fashion. Key topics include: • An introduction to FEM • Fundamentals and analysis capabilities of ANSYS® • Fundamentals of discretization and approximation functions • Modeling techniques and mesh generation in ANSYS® • Weighted residuals and minimum potential energy • Development of macro files • Linear structural analysis • Heat transfer and moisture diffusion • Nonlinear structural problems • Advanced subjects such as submodeling, substructuring, interaction with external files, and modification of ANSYS®-GUI Supplementary materials for this book may be downloaded from http://extras.springer.com. This convenient online feature, which includes color figures, screen shots and input files for sample problems, allows for regeneration on the reader's own computer. Students, researchers, and practitioners alike will find this an essential guide to predicting and simulating the physical behavior of complex engineering systems.

29. HÖHNE, T., KREPPER, E. and ROHDE, U. Application of CFD codes in nuclear reactor safety analysis. *Science and Technology of Nuclear Installations*. 2010. DOI 10.1155/2010/198758. Computational Fluid Dynamics (CFD) is increasingly being used in nuclear reactor safety (NRS) analyses as a tool that enables safety relevant phenomena occurring in the reactor coolant system to be described in more detail. Numerical investigations on single phase coolant mixing in Pressurised Water Reactors (PWR) have been performed at the FZD for almost a decade. The work is aimed at describing the mixing phenomena relevant for both safety analysis, particularly in steam line break and boron dilution scenarios, and mixing phenomena of interest for economical operation and the structural integrity. For the experimental investigation of horizontal two phase flows, different non pressurized channels and the TOPFLOW Hot Leg model in a pressure chamber was build and simulated with ANSYS CFX. In a common project between the University of Applied Sciences Zittau/Görlitz and FZD the behaviour of insulation material released by a LOCA released into the containment and might compromise the long term emergency cooling systems is investigated. Moreover, the actual capability of CFD is shown to contribute to fuel rod bundle design with a good CHF performance.
30. HÖHNE, Thomas. CFD Simulation of Thermal-Hydraulic Benchmark V1000CT-2 Using ANSYS CFX. *Science and Technology of Nuclear Installations*. 2009. DOI 10.1155/2009/835162. Plant measured data from VVER-1000 coolant mixing experiments were used within the OECD/NEA and AER coupled code benchmarks for light water reactors to test and validate computational fluid dynamic (CFD) codes. The task is to compare the various calculations with measured data, using specified boundary conditions and core power distributions. The experiments, which are provided for CFD validation, include single loop cooling down or heating-up by disturbing the heat transfer in the steam generator through the steam valves at low reactor power and with all main coolant pumps in operation. CFD calculations have been performed using a numerical grid model of 4.7 million tetrahedral elements. The Best Practice Guidelines in using CFD in nuclear reactor safety applications has been

used. Different advanced turbulence models were utilized in the numerical simulation. The results show a clear sector formation of the affected loop at the downcomer, lower plenum and core inlet, which corresponds to the measured values. The maximum local values of the relative temperature rise in the calculation are in the same range of the experiment. Due to this result, it is now possible to improve the mixing models which are usually used in system codes.

31. *ANSYS CFX - Documentation*. 2019.
32. BREITKREUTZ, Harald, RÖHRMOSER, Anton and PETRY, Winfried. 3-dimensional coupled neutronic and thermal-hydraulic calculations for a compact core combining MCNPX and CFX. *IEEE Transactions on Nuclear Science*. 2010. DOI 10.1109/TNS.2010.2086479. The neutronic Monte Carlo code MCNPX and the thermohydraulic CFD code CFX have been coupled to satisfy the increasing demand for 3-dimensional results with high spatial resolution in nuclear reactor physics. In a first step, results for an evolute shaped fuel plate of a symmetric compact core and an attached cooling channel in the fuel element of FRM II were regarded. ©2009 IEEE.
33. KLIEM, S and ROHDE, U. Prototype coupling of the CFD software ANSYS CFX with the 3D neutron kinetic code model DYN3D. In : *PHYSOR 2010 – Advances in Reactor Physics to Power the Nuclear Renaissance*. 2010. The CFD code ANSYS CFX has been coupled with the neutron-kinetic core model DYN3D. ANSYS CFX calculates the fluid dynamics and related transport phenomena in the reactor's coolant and provides the corresponding data to DYN3D. In the fluid flow simulation of the coolant, the core itself is modeled within the porous body approach. DYN3D calculates the neutron kinetics and the fuel behavior including the heat transfer to the coolant. The physical data interface between the codes is the volumetric heat release rate into the coolant. In the prototype that is currently available, the coupling is restricted to single-phase flow problems. In the time domain an explicit coupling of the codes has been implemented so far. Steady-state and transient verification calculations for a small-size test problem confirm the correctness of the implementation of the prototype coupling. This test problem was a mini-core consisting of nine real-size fuel assemblies. Comparison was performed with the DYN3D stand-alone code. In the steady state, the effective multiplication factor obtained by the ANSYS CFX/DYN3D codes shows a deviation of 9.8 pcm from the DYN3D stand-alone solution. This difference can be attributed to the use of different water property packages in the two codes. The transient test case simulated the withdrawal of the control rod from the central fuel assembly at hot zero power. Power increase during the introduction of positive reactivity and power reduction due to fuel temperature increase are calculated in the same manner by the coupled and the stand-alone codes. The maximum values reached during the power rise differ by about 1 MW at a power level of 50 MW Beside the different water property packages, these differences are caused by the use of different flow solvers.
34. RUELLE, David and TAKENS, Floris. On the nature of turbulence. *Communications in Mathematical Physics*. 1971. DOI 10.1007/BF01646553. A mechanism for the generation of turbulence and related phenomena in dissipative systems is proposed.
35. ARGYROPOULOS, C. D. and MARKATOS, N. C. *Recent advances on the numerical modelling of turbulent flows*. 2015. This paper reviews the problems and successes of computing turbulent flow. Most of the flow phenomena that are important to modern technology involve turbulence. The review is concerned with methods for turbulent flow computer predictions and their applications, and describes several of them. These computational methods are aimed at simulating either as much detail of the turbulent

motion as possible by current computer power or, more commonly, its overall effect on the mean-flow behaviour. The methods are still being developed and some of the most recent concepts involved are discussed. Some success has been achieved with two-equation models for relatively simple hydrodynamic phenomena; indeed, routine design work has been undertaken during the last three decades in several applications of engineering practise, for which extensive studies have optimised these models. Failures are still common for many applications particularly those that involve strong curvature, intermittency, strong buoyancy influences, low-Reynolds-number effects, rapid compression or expansion, strong swirl, and kinetically-influenced chemical reaction. New conceptual developments are needed in these areas, probably along the lines of actually calculating the principal manifestation of turbulence, e.g. intermittency. A start has been made in this direction in the form of "multi-fluid" models, and full simulations. The turbulence modelling approaches presented here are, Reynolds-Averaged Navier-Stokes (RANS), two-fluid models, Very Large Eddy Simulation (VLES), Unsteady Reynolds-Averaged Navier-Stokes (URANS), Detached Eddy Simulation (DES) and some interesting, relatively recent, hybrid LES/RANS techniques. A large number of relatively recent studies are considered, together with reference to the numerical experiments existing on the subject. The authors hope that they provide the interested reader with most of the appropriate sources of turbulence modelling, exhibiting either as much detail as it is possible, by means of bibliography, or illustrating some of the most recent developments on the numerical modelling of turbulent flows. Thus, the potential user has the appropriate information, for him to select the suitable turbulence model for his own case of interest.

36. H.K. MYONG, N. Kasagi. A new approach to the improvement of k-eps turbulence model for a wall bounded shear flows. *JSME Internaitonal Journal*. 1990. An improved near- wall k-e turbulence model is proposed considering the two chara cterist ic length sca les for the dissipation rate. one very near the wall and the other remote from the wall. which are then related to the lengt h sca le for turbulent momentum tr ansfer. Consequently, the functio n I. included in the eddy diffusivity model represents two distinct physical effects of low turbulent Reynolds number and wall proximity. The present k-e model is evaluated for its app lication to fully developed turbulent pipe and channel flows and found to resolve two serious weaknes- ses common to previous k-e models ; i. e., it correctly predicts the wall-limiting behavior of the maj or turbu lence quantities such as Reynolds st ress, turbulen t kinetic energy and its dissipation rate near the wall. and the distributions of eddy diffusivity of momentum and turbulen t kinetic energy even in the region far from the wall.
37. WILCOX, D. C. Formulation of the k-w Turbulence Model Revisited. *AIAA Journal*. 2008. DOI 10.2514/1.36541. This paper presents a reformulated version of the author's k-!model of turbulence. Revisions include the addition of just one new closure coefficient and an adjustment to the dependence of eddy viscosity on turbulence properties. The result is a significantly improved model that applies to both boundary layers and free shear flows and that has very little sensitivity to finite freestream boundary conditions on turbulence properties. The improvements to the k-! model facilitate a significant expansion of its range of applicability. The new model, like preceding versions, provides accurate solutions for mildly separated flows and simple geometries such as that of a backward-facing step. The model's improvement over earlier versions lies in its accuracy for even more complicated separated flows. This paper demonstrates the enhanced capability for supersonic flow into compression corners and a hypersonic shock-wave/ boundary-layer interaction. The excellent

agreement is achieved without introducing any compressibility modifications to the turbulence model.

38. KALITZIN, Georgi, MEDIC, Gorazd and XIA, Guoping. Improvements to SST turbulence model for free shear layers, turbulent separation and stagnation point anomaly. In : . 2016. Three modifications to the SST model are investigated. They are aimed at improving the recovery for turbulent separation, the near wall behavior and the stagnation region. The modification for suppressing the eddy-viscosity build up in the stagnation region follows the derivation by Durbin. However, here we guarantee that realizability is enforced only where principal stresses violate the realizability condition.
39. DURY, Trevor V. Heat transfer to a heavy liquid metal in curved geometry: Code validation and CFD simulation for the Megapie lower target. *Nuclear Instruments and Methods in Physics Research, Section A: Accelerators, Spectrometers, Detectors and Associated Equipment*. 2006. DOI 10.1016/j.nima.2006.02.131. The ESS and SINQ Heat Emitting Temperature Sensing Surface (HETSS) mercury experiments have been used to validate the Computational Fluid Dynamics (CFD) code CFX-4 employed in designing the lower region of the international liquid-metal cooled Megapie target, to be installed at SINQ, PSI, in 2006. Conclusions were drawn on the best turbulence models and degrees of mesh refinement to apply, and a new CFD model of the Megapie geometry was made, based on the CATIA CAD design of the exact geometry constructed. This model contained the fill and drain tubes as well as the bypass feed duct, with the differences in relative vertical length due to thermal expansion being considered between these tubes and the window. Results of the mercury experiments showed that CFD calculations can be trusted to give peak target window temperature under normal operational conditions to within about ±10%. The target nozzle actually constructed varied from the theoretical design model used for CFD due to the need to apply more generous separation distances between the nozzle and the window. In addition, the bypass duct contraction approaching the nozzle exit was less sharp compared with earlier designs. Both of these changes modified the bypass jet penetration and coverage of the heated window zone. Peak external window temperature with a 1.4 mA proton beam and steady-state operation is now predicted to be 375 °C, with internal temperature 354.0 °C (about 32 °C above earlier predictions). Increasing bypass flow from 2.5 to 3.0 kg/s lowers these peak temperatures by about 12 °C. Stress analysis still needs to be made, based on these thermal data. © 2006 Elsevier B.V. All rights reserved.
40. ČOMOR, J. J., STEVANOVIĆ, Ž, RAJČEVIĆ, M. and KOŠUTIĆ, D. Modeling of thermal properties of a TeO2 target for radioiodine production. *Nuclear Instruments and Methods in Physics Research, Section A: Accelerators, Spectrometers, Detectors and Associated Equipment*. 2004. Vol. 521, no. 1, p. 161–170. DOI 10.1016/j.nima.2003.11.147. Three radionuclides of iodine (120I,123I and124I) are of great interest for modern nuclear medical diagnostics. They can be all produced by the (p,n) nuclear reaction using isotopically enriched solid TeO2targets. The produced radioiodine can be rapidly separated from the target material by dry-distillation from the melted target after the irradiation. Since TeO2has low thermal conductivity, the most critical issue in the design of a production target is the provision of its effective cooling in order to avoid melting of the oxide layer during the irradiation. A compact solid target irradiation system (COSTIS) has been designed for the irradiation of TeO2targets, suitable for routine production of radioiodine. The target is a circular Pt-disk that carries the TeO2melted into a circular grove in the center of

the disk. The target coin is manually inserted into COSTIS, fixed pneumatically in the irradiation position, released remotely after irradiation and falls down driven by gravity into a transport container. The engineering design of the cavity for helium cooling of the front face of TeO2and the impinging water jet cooling the back face of the target disk was done based on a simulation of the thermal behavior of the target during the irradiation. A straightforward numerical method for the prediction of the thermal properties of the solid target has been developed. The approach is based on calculations without using the common practice of Prandtl and Nusselt empirical correlation. The fluid flow description in the boundary layer was refined in such a way, that the heat flux, exchanged between the solid and fluid, is obtained directly from Fourier law. The governing equations are based on the local thermodynamic equilibrium and conservation equation of mass, momentum and energy. In order to solve the set of governing equations, the finite-volume method is used. This procedure gives rapid answers whether the proposed geometry satisfies the design criteria. © 2003 Elsevier B.V. All rights reserved.

41. JUNG, N S, KIM, S J, KIM, J H, CHUN, K S and CHOI, H D. Thermal Analysis of Thallium Solid Target of Cyclotron. . 2006. P. 3–4.
42. SONG, T.Y. Thermal and Stress Analysis of Hyper Target System. *Korea Atomic Energy Research Institute*. 2000.
43. GRAHN, Alexander, KLIEM, Sören and ROHDE, Ulrich. Coupling of the 3D neutron kinetic core model DYN3D with the CFD software ANSYS-CFX. *Annals of Nuclear Energy*. 2015. DOI 10.1016/j.anucene.2014.12.015. This article presents the implementation of a coupling between the 3D neutron kinetic core model DYN3D and the commercial, general purpose computational fluid dynamics (CFD) software ANSYS-CFX. In the coupling approach, parts of the thermal hydraulic calculation are transferred to CFX for its better ability to simulate the three-dimensional coolant redistribution in the reactor core region. The calculation of the heat transfer from the fuel into the coolant remains with DYN3D, which incorporates well tested and validated heat transfer models for rod-type fuel elements. On the CFX side, the core region is modeled based on the porous body approach. The implementation of the code coupling is verified by comparing test case results with reference solutions of the DYN3D standalone version. Test cases cover mini and full core geometries, control rod movement and partial overcooling transients.
44. FAUGL, T., STOKELY, M., WIELAND, BOLOTNOV, I., DOSTER, J., PEEPLES, J. and POORMAN, M. Modeling a Water Target with Proton Range and Target Density Coupling. In : . North Carolina State University;BTI Targetry, LLC, 2014.
45. O'BRIEN, E. M., DOSTER, J. M., NORTIER, F. M., OLIVAS, E. R. and STOKELY, M. H. Two-way multi-physics coupling for modeling high power RbCl isotope production targets. *Nuclear Instruments and Methods in Physics Research, Section B: Beam Interactions with Materials and Atoms*. 2018. DOI 10.1016/j.nimb.2018.07.022. This work shows successful first application of two-way multi-physics coupling to model RbCl targets in a three-stacked target configuration used at Los Alamos National Laboratory's (LANL) Isotope Production Facility (IPF). Targets are known to melt at production level beam currents and as in-beam monitoring of the targets in this configuration is not possible, high-fidelity simulation has been utilized to gain insight into target thermal behavior. Thermal hydraulic modeling was performed with ANSYS CFX and particle transport with the Monte Carlo N-Particle (MCNP) code. Multi-physics coupling of these two codes was employed to fully capture the highly coupled nature of the problem physics. Both transient and equilibrium thermal hydraulic results

were obtained using this process. The equilibrium thermal hydraulic results were then employed to predict measured 82Sr yields in molten RbCl targets. This technique demonstrates promise as a tool to investigating, understanding, and enhancing high power targetry behavior and limitations.

46. DO CARMO, Sergio, DE OLIVEIRA, Pedro and ALVES, Francisco. *A Target-Temperature Monitoring System for Cyclotron Targets: Safety Device and Tool to Experimentally Validate Targetry Studies*. 2018.
47. SHASHIKANT T and BINDU, R.S. Effect of Mesh Size on Finite Element Analysis of Plate Structure. *Certified International Journal of Engineering Science and Innovative Technology*. 2008. In finite element analysis, mesh size is a critical issue. It closely relates to the accuracy, computing time and efforts required for meshing of finite element models, which determines their complexity level. This paper presents study of the effects of mesh size on accuracy of numerical analysis results. Based on these results the guidelines for choosing the appropriate mesh strategy in finite element modelling are provided. The static and buckling analysis is carried out to know the effects of mesh sizes by using Femap and NX-Nastran. The model under study is of a structure made up of steel plate. Index Terms— Finite element analysis, mesh size, static analysis, buckling analysis. I. INTRODUCTION In finite element analysis (FEA), the accuracy of the FEA results and required computing time are determined by the finite element size (mesh density). According to FEA theory, the FE models with fine mesh (small element size) yields highly accurate results but may take longer computing time. On the other hand, those FE models with coarse mesh (large element size) may lead to less accurate results but smaller computing time. Also, small element size will increase the FE model's complexity which is only used when high accuracy is required. Large element size, however, will reduce the FE model's size and is extensively used in simplified models in order to provide a quick and rough estimation of designs. Due to its importance, in generating FEA models, the foremost problem is to choose appropriate elements size so that the created models will yield accurate FEA results while save as much computing time as possible. The objective of this paper is to present guidelines for choosing optimal element size for different types of finite element analyses. In order to achieve that goal, in this study, a series of static, and buckling analyses were performed on a structure model made up of plates to reveal the effects of the element size on the accuracy of the FEA results. The solver NX-Nastran and Femap pre and post-possessor, used for modeling and analyses involved in this work.
48. WAGNER, W., COOPER, J. R., DITTMANN, A., KIJIMA, J., KRETZSCHMAR, H.-J., KRUSE, A., MAREŠ, R., OGUCHI, K., SATO, H., STÖCKER, I., ŠIFNER, O., TAKAISHI, Y., TANISHITA, I., TRÜBENBACH, J. and WILLKOMMEN, Th. The IAPWS Industrial Formulation 1997 for the Thermodynamic Properties of Water and Steam. *Journal of Engineering for Gas Turbines and Power*. 2000. DOI 10.1115/1.483186. In 1997, the International Association for the Properties of Water and Steam (IAPWS) adopted a new formulation for the thermodynamic properties of water and steam for industrial use. This new formulation, called IAPWS Industrial Formulation 1997 for the Thermodynamic Properties of Water and Steam (IAPWS-IF97), replaces the previous industrial formulation, IFC-67, that had formed the basis for power-plant calculations and other applications in energy engineering since the late 1960's. IAPWS-IF97 improves significantly both the accuracy and the speed of the calculation of the thermodynamic properties compared with IFC-67. The differences between IAPWS-IF97 and IFC-67 will require many users, particularly

boiler and turbine manufacturers, to modify design and application codes. This paper summarizes the need and the requirements for such a new industrial formulation and gives the entire numerical information about the individual equations of IAPWS-IF97. Moreover, the scientific basis for the development of the equations is summarized and the achieved quality of IAPWS-IF97 is presented regarding the three criterions accuracy, consistency along region boundaries, and computation speed. For comparison, corresponding results for the previous standard IFC-67 are also presented.

49. CHURCHILL, Stuart W. Free convection around immersed bodies. In : *HEDH Multimedia*. 2017.
50. LIENHARD, John. A Heat Transfer Textbook. *J Heat Transfer*. 2013. Vol. 108.
51. TABIB, Mandar V., ROY, Swarnendu A. and JOSHI, Jyeshtharaj B. CFD simulation of bubble column-An analysis of interphase forces and turbulence models. *Chemical Engineering Journal*. 2008. DOI 10.1016/j.cej.2007.09.015. 3D transient CFD simulations of bubble column have been performed for a wide range of superficial gas velocity on an industrially relevant cylindrical column and the CFD predictions have been compared with the experiments of Menzel et al. [T. Menzel, T. Weide, O. Staudacher, U. Onken, Reynolds stress model for bubble column reactor, Ind. Eng. Chem. Res. 29 (1990) 988-994]. Simulations have also been performed to understand the sensitivity of different interphase forces (drag, lift, turbulent dispersion and added mass). This work highlights the importance of choosing the C L value and the drag law in accordance with the bubble size. Further, a laboratory scale bubble column with three different spargers (perforated plate, sintered plate and single hole) has been simulated using three different turbulence closure (k-ε, RSM and LES) models, with the purpose of critically comparing their predictions with experimental data [M.R. Bhole, S. Roy, J.B. Joshi, Laser doppler anemometer measurements in bubble column: effect of sparger, Ind. Eng. Chem. Res. 45 (26) (2006) 9201-9207; A.A. Kulkarni, K. Ekambara, J.B. Joshi, On the development of flow pattern in a bubble column reactor: experiments and CFD, Chem. Eng. Sci. 62 (2007) 1049-1061]. It has been found that the RSM shows better agreement than the k-ε model in predicting the turbulent kinetic energy profiles. Comparatively, the LES has been successful in capturing the averaged behavior of the flow, while at some locations; it slightly over predicts the kinetic energy profiles. Further, it has been able to simulate the instantaneous vortical-spiral flow regime in case of sieve plate column, as well as, the bubble plume dynamics in case of single hole sparger. Thus, LES can be effectively used for study of flow structures and instantaneous flow profiles. © 2007 Elsevier B.V. All rights reserved.